NASA

Technical Memorandum **84936**

The GLAS Physical Inversion Method for Analysis of HIRS2/MSU Sounding Data

J. Susskind, J. Rosenfield, D. Reuter and M. T. Chahine

November 1982

Laboratory for Atmospheric Sciences
Modeling and Simulation Facility

National Aeronautics and Space Administration

Goddard Space Flight Center
Greenbelt, Maryland 20771

The GLAS Physical Inversion Method For Analysis of HIRS2/MSU Sounding Data

J. Susskind , J. Rosenfield* and D. Reuter**

Goddard Laboratory for Atmospheric Sciences
NASA/Goddard Space Flight Center
Greenbelt, MD 20771

and

M. T. Chahine

Jet Propulsion Laboratory
California Institute of Technology
Pasadena, CA 91109

*with MA/COM Sigma Data Services Corporation

**Resident Research Associate

Table of Contents

List of Tables

List of Figures

Introduction

HIRS2, a 20 channel infra-red sounder, and MSU, a 4 channel microwave sounder, were first launched on TIROS-N in November 1978 as an upgraded operational temperature sounding system. Essentially identical instruments have flown on NOAA-A and NOAA-C and are scheduled to fly on future operational satellites through the eighties. While HIRS2 and MSU were designed primarily for the purpose of measuring atmospheric temperature profiles, the observed radiances are also sensitive to other meteorological parameters such as sea-surface temperature, ground temperature, cloud height and cloud amount, ice extent over ocean, snow cover over land, etc.

In this report, we describe a physically based research oriented processing system for HIRS2/MSU data, developed at the Goddard Laboratory for Atmospheric Sciences (GLAS), which provides fields not only of temperature profiles but also of all of the above quantities. All parameters are retrieved in a mutually interacting fashion. Global retrievals have been produced for the period Jan 5 - Feb 2, 1979 at a resolution of 125 x 125 km. A preliminary analysis of the results shows the accuracy of the atmospheric temperature retrievals to be significantly better than those produced operationally during that period using statistical regression techniques. In addition, monthly mean fields of retrieved surface temperature, cloud cover, and ice and snow cover appear to be comparable to those retrieved from instruments such as AVHRR and SMMR which were designed primarily to measure these products.

In all cases, dedicated instruments have to contend with some form of "noise", the atmosphere and clouds if one wants to measure surface phenomena, the surface and the atmosphere if one wants to measure clouds, etc. While the HIRS2/MSU system is not particulary optimized for monitoring any of the quantities usually obtained by imagers, a physical retrieval method enabling

all quantities to be retrieved simultaneously both minimizes the residual effects of atmospheric and surface "noise" on the retrieved products and also produces fields of all quantities which are compatible with each other. The ability to retrieve climate parameters from the operational sounding system is all the more significant because this will allow continuous monitoring of climate parameters from 1978 on.

The physical based processing scheme for analysis of the HIRS2/MSU data is an outgrowth of research and experience that began with VTPR data on NOAA-2 and NOAA-4 [Jastrow and Halem, 1973; Halem and Susskind, 1977] and continued with work on HIRS/MSU data from NIMBUS 6 [Halem et al., 1978]. Earlier versions of the processing scheme for the HIRS2/MSU data on TIROS-N are described in Susskind and Rosenberg [1979] and Susskind and Rosenfield [1980]. The analysis procedures are based on the relaxation scheme and cloud filtering methods of Chahine [1970, 1974].

In the process of performing direct physical solution of the inversion problem, atmospheric and surface conditions are found which meet the requirement that the channel averaged radiances computed from these conditions agree with the observed radiances to within a specified error limit. Thus, errors in computation of radiances (hereafter called the forward problem) become a serious potential source of noise affecting the accuracy of the method. The accuracies obtained by various groups employing direct physical inversion techniques [Jastrow and Halem, 1973; Halem et al., 1978; Susskind and Rosenfield, 1980] imply the ability to compute expected satellite observations, given surface and atmospheric conditions, with a sufficient accuracy so as not to significantly degrade the retrievals. Nevertheless, doubts have been raised regarding the current state of the forward problem, that is, the accuracy with which our knowledge of atmospheric transmittance functions and our use of the

radiative transfer equation assumptions can reproduce the observed satellite radiances for given atmospheric and surface conditions.

McClatchey [1976] found bias errors of the order of 6°C between radiances observed in a number of 15 μm channels of the DMSP infra-red sounder and those calculated using colocated radiosonde observations. In all cases, computed radiances were larger than observed ones. Based on his calculations, he was one of the first to question whether radiative transfer calculations can be done in the infra-red region with sufficient accuracy to allow for direct physical inversion of infra-red sounder observations. Valovcin (1981) did a similar comparision for the 20μm water vapor sounding channels of the DMSP sounder and again found biases in the same sense of the order of 5°C for these channels. He suggested further studies of the forward problem to pinpoint the sources of these large errors. Weinreb (1979) at NOAA/NESS showed that significant empirical corrections had to be made to remove biases between observed and computed brightness temperatures for the HIRS instrument. No indication of the RMS difference between observed and computed radiances was given in Weinreb (1979) but he implies that better accuracy is needed before physically based retrievals can improve upon statistically based retrievals.

In first chapter of this report, we describe the radiative transfer calculations performed at GLAS for the HIRS2 and MSU sounders, and show, by direct comparison of satellite observations with those computed from colocated radiosonde observations, that agreement in both the infra-red and microwave channels can be obtained with sufficient accuracy to meet the needs for physically based retrievals yielding high accuracy, even in the presence of clouds. In the second chapter, a rapid algorithm for computing the channel averaged transmittance functions as a function of temperature profile, humidity profile, ozone profile, and zenith angle of observations is described. This algorithm,

which is used in the analysis of TIROS-N data, is shown to be sufficiently accurate so as not to significantly affect retrieval accuracy. In the third chapter, we describe the theory and application of the processing scheme used at GLAS to provide global retrievals (12000 retrievals per day) for the period Jan 5 - Feb 2, 1979. In the final chapter, we will show results indicating the accuracies of retrieved temperature profiles for the period as well as monthly mean fields of sea/land surface temperatures, cloud height and cloud amount, and microwave surface emissivity at 50.3 GHz, from which we deduce ice cover over ocean and snow cover over land. More detailed studies of these quantities, as well as a description of improvements to the processing scheme, will be given in future publications.

Chapter 1

An Accurate Radiative Transfer Model for the Direct Calculation of Brightness Temperatures for the HIRS2 and MSU Sounding Channels

1.1 The Radiative Transfer Equation - "The Forward Problem"

The radiance calculations used in the GLAS physical inversion method are based on the form of the radiative transfer equation for computing clear column radiances R_i, for sounding channel i, given by

$$R_i = \varepsilon_i B_i[T_s]\,\tau_i(P_s) + (1-\varepsilon_i)R_i^{\downarrow}\tau_i(P_s) + \rho_i' H_i \tau_i'(P_s) + \int_{\ln P_s}^{\ln \overline{P}} B_i[T(P)]\,\frac{d\tau}{d\ln P}\,d\ln P \qquad (1.1)$$

where ε_i is the surface emissivity averaged over sounding channel i, $B_i[T]$ is the mean Plank blackbody function, averaged over channel i, of the temperature T, $\tau_i(P)$ is the mean atmospheric transmittance from pressure P to the top of the atmosphere and evaluated at θ, the zenith angle of the observation, $R_i^{\downarrow}$ is an effective atmospheric emission downward flux, [Kornfield and Susskind, 1977], ρ_i' is the directional reflectance of the solar radiation, H_i is the channel averaged solar radiance striking the top of the atmosphere, and $\tau_i'(P_s)$ is an effective atmospheric transmittance of radiation from the sun, reflected from the earth's surface to the satellite [Susskind and Rosenfield, 1980]. The subscript s refers to the earth's surface. The integral, taken from the surface to the satellite pressure $\overline{P}$, represents the upwelling atmospheric emitted radiation, which is a mean value of the black-body function of atmospheric temperature weighted by the channel weighting function $d\tau_i/d\ln P$. Table 1 shows the channels, centers of the filter functions, peaks of the weighting functions, and other relevant information, for the channels on MSU and HIRS2. The HIRS2 and MSU channels used in the GLAS Physical inversion method are designated by *. The radiative transfer equation for a plane parallel homogeneous atmosphere expressed by equation (1.1) assumes atmospheric local thermodynamic equilibrium.

This assumption is reasonable for radiance calculations for all channels but HIRS2 channel 17, which contains considerable emission from pressures lower than 1 mb. For this reason, channel 17 was not included in this study.

Table 1.1

HIRS2 and MSU Channels

Channel	$\nu(cm^{-1})$	Peak of $d\tau/d\ln p$ (mb)	Peak of $Bd\tau/d\ln p$ (mb)
H1	668.40	30	20
*H2	679.20	60	50
H3	691.10	100	100
*H4	703.60	280	360
H5	716.10	475	575
H6	732.40	725	875
H7	748.30	Surface	Surface
H8	897.70	Window, sensitive to water vapor	
H9	1027.90	Window, sensitive to O_3	
H10	1217.10	Lower tropospheric water vapor	
H11	1363.70	Middle tropospheric water vapor	
H12	1484.40	Upper tropospheric water vapor	
*H13	2190.40	Surface	Surface
*H14	2212.60	650	Surface
*H15	2240.10	340	675
H16	2276.30	170	425
H17	2310.70	15	2
*H18	2512.00	Window, sensitive to solar radiation	
*H19	2671.80	Window, sensitive to solar radiation	
*M1	50.30a	Window, sensitive to surface emissivity	
*M2	53.74a	500	
*M3	54.96a	300	
*M4	57.95a	70	

a values in GH_Z

1.2. Calculation of Atmospheric Transmittances

The atmospheric transmittance functions $\tau_1(P)$, contain components coming from attenuation by discrete lines of absorbing gases, $\tau_{1L}(P)$, and also from broad-banded continuum absorption features. The component coming from discrete lines can be calculated by line-by-line calculations according to

$$\tau_{1L}(P,\theta) = \int d\nu \; F_1(\nu) \; e^{-\int_{z(P)}^{\infty} \sum_L k_L(\nu,z) \; C_L(z)\rho(z) \; dz \sec\theta} \qquad (1.2)$$

where $F(\nu)$ is a normalized channel response function, $k_L(\nu, z)$ is the absorption coefficient of line L evaluated at the temperature and pressure of height z, $c_L(z)$ is the molecular mixing ratio for the gas to which line L belongs, ρ is the density of air, and θ is the zenith angle of observation. The evaluation of $k_L(\nu, z)$ depends not only on the set of line parameters used [McClatchey et al., 1973] but also on assumptions regarding the temperature dependence of the Lorentz half width and the nature of the line shape. Finally, the results also depend on the numerical quadrature used in the computation of equation (1.2).

All calculations for the HIRS2 channel transmittances were made as in Susskind and Searl (1978) using the 1978 version of the AFGL line parameter tape [Rothman, 1978]. The MSU transmittance functions were calculated in a similar manner, but using a Van-Vleck Weiskopf line shape and the overlapping line theory given by Rosenkranz (1975) in the case of O_2 absorption. Computations were done with a 64 level atmosphere and a frequency spacing of .002 cm^{-1} for the HIRS2 channels and .00006 cm^{-1} for the MSU channels. Filter functions for HIRS2 on TIROS-N were provided by NOAA/NESS. The MSU channels were treated as having rectangular response with the specified centers and half-widths.

The CO_2 line shape was taken to be sub-Lorentz as described by Susskind and Mo (1978). One significant modification made to the calculations of Susskind and Searl (1978) was to include induced emission in the computation of the temperature dependence of the line strengths

$$\frac{S(T)}{S(T_S)} = \frac{Q_V(T_S)\, Q_R(T_S)}{Q_V(T)\, Q_R(T)} \times \frac{e^{-1.439\, E''/T}\left[1 - e^{-1.439\nu/T}\right]}{e^{-1.439\, E''/T_S}\left[1 - e^{-1.439\nu/T_S}\right]} \qquad (1.3)$$

where E", Q_V and Q_R are defined in McClatchey et al., (1973). Neglect of the induced emission factor, $(1 - e^{-1.439\nu/T})/(1 - e^{1.439\nu/T_S})$, as done in

McClatchey et al., (1973) and Susskind and Searl (1978), decreases the intensity of lines at low temperatures relative to high temperature. For example, at ν=650 cm^{-1}, the intensity of a line at 220K is underestimated relative to tive to its intensity at 300 K by 3%. Such an error has the effect of broadening the weighting functions of channels sounding the tropopause region.

The total transmittance function $\tau_i(P)$ is taken as

$$\tau_i(P) = \tau_{iL}(P)\, \tau_{iN}(P)\, \tau_{iW}(P)\, \tau_{ia}(P) \qquad (1.4)$$

where τ_N, τ_W and τ_a represent continuum absorption due to N_2, water vapor, and aerosols. Water vapor continuum and Nitrogen continuum absorption are treated as in Susskind and Searl (1978). Aerosol absorption and scattering is treated according to

$$\tau_a(P) = e^{-k_a(P)\sec\theta} \qquad (1.5)$$

where $k_a(P)$ is the sum of the aerosol scattering and aerosol absorption optical thickness from pressure P to the top of the atmosphere. The aerosol model used is based on the tropospheric light haze model and calculations of Wang and Domoto (1974). The total optical depth of the tropospheric aerosols is taken as .01 for nadir viewing in the 15μm channels. The optical depth falls off with a 1.2 km scale height. An additional homogeneous stratospheric aerosol layer between 12 and 20 km was added with total optical depth 30% of that of the tropospheric layer [Wang, 1975]. Optical depths in the 4.3μm region were taken to be a factor of three greater than in the 15μm region, giving a total nadir optical depth of .039 for the 4.3μm channels.

1.3. Need for Rapid Transmittance Algorithms

Line-by-line transmittance calculations using equation (1.2) take about 2 minutes CPU (on a 5 MIPS machine) per channel per sounding for the HIRS2

channels and is computationally impractical for global analysis of satellite data (≈ 12000 soundings per day). It is therefore necessary to have a rapid algorithm which can reproduce the transmittances, including their dependence on the important variables, the temperature-humidity-ozone profile and zenith angle of observation, to a desired accuracy. Given an analytical form of the approximate transmittance model, line by line calculations are used both to generate empirical coefficients and to verify the model. An examination of equation (1.2) for the special case of monochromatic transmittances $\tau_\nu(P,\theta)$ shows that

$$\tau_\nu(P,\theta) = \prod_I \tau_{\nu I}(P)^{\sec\theta} \tag{1.6a}$$

$$\text{and } \tau_\nu(P,\theta) = \tau_\nu(P',\theta)\ \tau_\nu(P,P',\theta) \tag{1.6b}$$

where $\tau_{\nu I}(P)$ is the vertical monochromatic transmittance from pressure P to the top of the atmosphere due to absorption from molecular species I, $P > P'$, and $\tau_\nu(P', P,\theta)$ is the monochromatic transmittance from pressure P to P' at zenith angle θ. These equations are not applicable for channel averaged transmittances, but they suggest the following form of a rapid algorithm which is analogous to equations 6a and 6b:

$$\bar{\tau}_{iL}(P_\ell,\theta) = \prod_{j=1}^{\ell} \bar{\tau}_{iF}(P_j,P_{j-1},\theta)\ \bar{\tau}_{iO}(P_j,P_{j-1},\theta)\ \bar{\tau}_{iW}(P_j,P_{j-1},\theta) \tag{1.7}$$

where $\tau_{iL}(P_\ell,\theta)$, the model discrete line transmittance for channel i through a path from pressure P_ℓ to the top of the atmosphere at zenith angle θ, is given as the product of effective channel averaged transmittances through all individual layers from the top of the atmosphere to pressure P_ℓ. The effective layer transmittances, in turn, are modelled as products of three components. The first, τ_{iF}, is the transmittance due to the gases assumed to have

fixed concentrations, the second, τ_{1O}, is the effective transmittance due to absorption from ozone; and the third, $\bar{\tau}_{1W}$, is the effective transmittance due to absorption from water vapor. The models for $\bar{\tau}_{1F}$, $\bar{\tau}_{1O}$, and $\bar{\tau}_{1W}$ will be discussed in chapter 2. In all cases, model coefficients are generated at a fixed set of angles and the logarithm of the effective layer transmittance is taken as being linear in secant θ. $\bar{\tau}_{1L}(P)$ is used in equation (1.4) in place of $\tau_{1L}(P)$.

1.4. Forward Calculation of Radiances

In this section, we assume a given temperature, humidity, and ozone profile and compute the transmittance function as described previously. The radiances are calculated by numerical integration of equation (1.1) using a 64 level atmosphere and a Simpson's quadrature rule. For infra-red channels, the surface emissivity ε_1 is taken to have the values of .98 over ocean for channels in the 12-15μm region and .96 over ocean for channels in the 4.3-3.7μm region [Wolfe, 1965]. Over land, the emissivity is taken as .95 and .85 for the long and short wave channels respectively. The effective downward flux $R_1\downarrow$ is modeled according to Kornfield and Susskind (1977) as

$$R_1\downarrow = F_1 B_1(T_S)\ [1-\tau_1(P_S)] \tag{1.8}$$

The values of F_1 found from this model for the HIRS2 channels are .71, .49, .42, and .55 for channels 6, 7, 13, and 14 respectively, and 1.0 for all other channels. For the microwave channels, the surface emissivity is calculated from the observation of MSU channel 1 according to

$$\varepsilon = \frac{R_1 - \int T d\tau - R_1\downarrow \tau_1(P_S)}{[T_S - R_1\downarrow]\ \tau_1(P_S)} \tag{1.9}$$

where R_1 is the observed brightness temperature for MSU channel 1, $R_1\downarrow$ is the

computed downward flux using the temperature-humidity profile, and $\tau_1(P_s)$ is the surface transmittance for microwave channel 1. The downward flux for microwave channels is averaged over all angles using an approximation based on monochromatic transmittances which are linear in the secant of the zenith angle.

1.5. Accounting for the Effects of Clouds on the Infra-red Observations

Infra-red radiation is highly attenuated by clouds in the field of view. The out-going radiation in cloudy conditions is a complicated function of the properties of the clouds as well as the other atmospheric and surface conditions already discussed. In the analysis of sounding data, we do not attempt to compute the expected outgoing radiation as a function of cloud properties. Instead we use a procedure to estimate or "reconstruct" the radiance which would have been observed if no clouds were in the field of view by simultaneous analysis of observations in two adjacent fields of view [Smith, W. L., 1968; Chahine, M. T., 1974]. One retrieval is performed in a 125 x 125 km area. For each area, we separate the many HIRS2 observations (20 x 20 km resolution at nadir) in the area into two groups, one set containing the half with the warmest observations in the 11μm window, the other set containing the coldest observations. Radiances for all spots in each set are averaged together for each channels to give representative observations in each "field of view". The observations in the two fields of view are used to provide reconstructed clear column radiances. The MSU observations assigned to the 125 x 125 km area are those of the closest MSU spot to the center of the 125 x 125 km box. No cloud correction is made to the MSU observations. Atmospheric and surface conditions are then found which when substituted into equation (1.1) match the reconstructed clear column radiances and microwave radiances for the spot. We will use the same set of observations in the comparison of observed and computed brightness temperatures using colocated radiosonde information.

The infra-red clear column brightness temperatures are reconstructed by making the assumption that the conditions in both fields of view are otherwise identical except for percentage cloud cover, α. The reconstructed clear column radiance is then given by

$$R_1 = R_{1,1} + \eta \ (R_{1,1} - R_{1,2}) \tag{1.10}$$

where $R_{1,J}$ is the observation for channel 1 in the field of view J and η is a parameter given by $\alpha_1/(\alpha_2-\alpha_1)$, where α_1 and α_2 are the cloud fractions in the two fields of view. In analysis of the sounding data, to be described in chapter 3, η is determined using observations in HIRS2 channel 13 and MSU channel 2. The microwave observations are included in the calculation to minimize errors in the determination of η due to incorrect estimates of the temperature profile. For the purposes of this study, where the temperature profile is known, the parameter η, which is independent of channel, is determined according to

$$\eta = \frac{R^{cc}_{13} - R_{13,1}}{R_{13,1} - R_{13,2}} \tag{1.11}$$

where R^{cc}_{13} is computed clear-column radiance for channel 13, using the radiosonde temperature profile.

According to equation (1.10), a value of $\eta = 0$ corresponds to field of view 1 (always taken as the field of view containing the larger radiance in the 11μm window channel) being clear, while a value of $\eta = -.5$ corresponds to both fields of view being clear.

If the observed channel 13 brightness temperatures in both fields of view differ by less than 1°C and $|\eta|<4$, η is set equal to $-.5$. In this case, both fields of view are assumed to be clear and the clear column radiance is given

by the average of the observations in both fields of view. If a value of $\eta \leq 0$ is obtained from equation (1.11) but the difference of the channel 13 brightness temperatures is greater than 1°, η is set equal to zero.

In the GLAS retrieval procedure for the HIRS2/MSU data, atmospheric and surface properties are found, which, when substituted into equation (1.1), match the reconstructed clear column radiances, obtained from equations (1.10) and (1.11). Using the the same procedure, we compare reconstructed clear column radiances with those computed from radiosonde conditions colocated with the satellite observations. Two sets of statistics will be presented: cases determined to be clear from eq. (1.11), and cases determined to be cloudy. In cloudy cases, the computed clear column radiance for channel 13 is artificially fixed to agree with the reconstructed clear column radiance by use of equations (1.10) and (1.11). In clear conditions, most often represented by $\eta = -.5$ as a result of homogeneity in both fields of view, a reasonable estimate of the accuracy of the calculations for channel 13 is obtained.

1.6. Comparison of observed and computed brightness temperatures

In this section, we compare the brightness temperatures calculated for the HIRS2 and MSU channels from rawinsonde temperature-humidity profiles with observations closely colocated in space and time. The radiosonde profiles used in the comparison are a select set of oceanic radiosondes [Phillips et al., 1979] which are also colocated in space by 110 km and in time by 3 hrs to the satellite observations. Only those radiosondes reporting temperatures at all mandatory levels from 1000 mb - 30 mb and humidities from 1000 - 500 mb were used in the comparison. The temperature above the highest radiosonde report was fixed at the values of the stratospheric analysis produced by the NMC Upper Air Branch. In cases where the analysis did not extend to 1 mb, the temperature profile was extrapolated to climatological 1 mb values. Comparisons

were limited to oceanic regions to minimize the effects of uncertainties in the surface temperature on the computed radiances.

Given the radiosonde temperature and humidity profile, brightness temperatures for the temperature sounding IR channels on HIRS2 were calculated according to equation (1.1). The temperature profile was interpolated to 64 levels assuming temperature to be linear in the logarithm of the pressure between the mandatory levels. The surface temperature was taken to be the climatological sea-surface temperature. The specific humidity was interpolated between mandatory levels assuming a P^n dependence. A specific humidity corresponding to a climatological water vapor mixing ratio of 3 ppmv was assumed at and above 100 mb. Zonally averaged climatological ozone profiles were use to compute the ozone component of the transmittance.

Two sets of statistics were calculated comparing observed and computed radiances. The first sample represents comparisons made only in those cases where at least one field of view was found to be clear, that is $\eta \leq 0$. The observed radiances in this case correspond to either the average or the warmer of the radiances in the two fields of view. The second sample contains only partially cloudy cases, $\eta > 0$, in which case comparisons were made between radiances reconstructed from eqns. (1.10) and (1.11) and computed clear column radiances. The first set of statistics, namely clear cases, is a measure primarily of the accuracy of the forward problem calculation. The second set, cloudy cases, is also a measure of the method's ability to account for cloud effects.

Clear Case

Table 1.2 gives the statistical comparisons relating the observed brightness temperatures with those computed using colocated radiosonde information for a set of 74 clear profiles from Jan-Feb 1979. The first two columns indicate the chan-

nel number and characteristic frequency of the channel as shown in Table 1.1. In order to minimize the effects of solar radiation, a subset of 21 cases occuring at night were used for comparison in channels 18 and 19, the two shortwave window channels and 8, the longwave window channel. While channel 8 is not affected by solar radiation, the subset of night cases was taken for consistency of the results with those in the two shortwave windows.

The third and fourth columns show the untuned mean and standard deviation of the differences between computed and observed brightness temperatures for each of the channels. The average absolute value of the mean difference is .68° C and the avarage standard deviation is 1.11° C. The largest standard deviations in the infra-red occur in channels 1-3 and 16, which are most sensitive to the temperature profile above 20 mb, not well monitored by radiosondes, and in the window channels, 8, 18, and 19, which are most sensitive to the sea-surface temperature, fixed at climatology. Typical deviations of sea-surface temperatures from their climatological values can be up to 2° C. The standard deviations in the remainder of the channels is less than 1°, with the exception of channel 7, which also is affected somewhat by errors in the climatological sea surface temperature. The standard deviations in the microwave channels are slightly larger than in infra-red channels sounding comparable portions of the atmosphere. Perfect "agreement" is forced in microwave channel 1 by the surface emissivity determined according to equation (1.9). At least part of the random component of the differences between observed and

TABLE 1.2

COMPARISON OF OBSERVED AND COMPUTED BRIGHTNESS TEMPERATURES (°C)

CLEAR CASES JAN - FEB 1979 (74 COLOCATIONS)

		UNTUNED			TUNED			
CH	ν (cm^{-1})	MEAN (COMP-OBS)	STD DEV	ε	MEAN (COMP-OBS)	STD DEV	STD DEV OBS	STD COMP
1	668.4	1.55	2.37	0	1.55	2.37	2.82	2.83
* 2	679.2	-.33	1.19	0	-.33	1.19	3.86	3.81
3	691.1	1.42	1.28	0	1.42	1.28	3.60	2.96
* 4	703.6	1.87	.92	.12	.03	.70	2.32	2.54
5	716.1	.66	.56	.03	.04	.57	4.31	4.17
6	732.4	.26	.70	.015	-.17	.70	5.19	5.03
7	748.3	.33	1.05	.04	-.37	1.05	5.07	4.74
**8	897.7	-.50	1.86	0	-.50	1.86	5.26	4.25
*13	2190.4	-.20	.70	0	-.20	.70	6.97	6.83
*14	2212.6	.86	.68	.04	.05	.65	7.09	7.19
*15	2240.1	.85	.70	.035	.05	.66	6.09	6.28
16	2276.3	.39	2.12	0	.39	2.12	2.84	3.38
**18	2512.0	.03	1.30	0	.03	1.30	6.74	6.36
**19	2671.8	-.09	1.33	0	-.09	1.33	6.32	5.85
*M1(b)	50.30a	0	0	0	0	0	10.66	10.66
*M2	53.74a	.66	.89	.035	-.07	.84	6.93	6.61
*M3	54.96a	1.57	1.20	.10	.11	.96	3.87	3.83
*M4	57.95a	.03	1.33	0	.03	1.33	7.45	6.93

a - values in GHz
b - used to determine emissivity
* - used in the GLAS retrieval systems for temperature sounding
** - 21 night cases only

computed brightness temperatures is due to sampling differences between radiosonde and satellite observations in space and time and errors in the radiosondes reports themselves.

It is apparent from column 3 of Table 1.2 that significant bias errors exist in a number of the sounding channels. Biases in channels sensitive to the surface or upper stratospheric temperatures may result in part from incorrect specifications of the appropriate conditions. Nevertheless, it is clear that atmospheric attenuation is underestimated in a number of channels, causing computed brightness temperatures to be systematically warm.

As shown in previous studies [Jastrow and Halem, 1973; Weinreb, 1979], systematic errors can be removed by empirical tuning of the transmittance functions. We considers the following form

$$\tau_i(P) = \tau_i(P)^{1+\varepsilon_i} \qquad (1.12)$$

which is equivalent to multiplying the effective channel optical depths by $1+\varepsilon_i$.

Tuning coefficients were found for channels, 4-7, 13-15, and M2-M4 which minimized the bias in the brightness temperatures errors computed in a sample of 20 clear cases taken from the first two weeks of January. The tuning coefficients obtained for these channels are shown in column 5 of Table II. The mean and standard deviation of the errors of the computed brightness temperatures using the tuned transmittances for the whole period are shown in columns 6 and 7 of the table. No attempt was made to tune channels sensitive to the stratosphere or the surface. The empirical tuning coefficients found in Table 1.2 are similar to those found by Weinreb (1979). In all cases, the tuning coefficients are positive, indicating the need for additional attenuation to that included in the calculations.

The tuning coefficients determined from data of the first two weeks of the period leave small biases when used on the whole sample. The standard deviation of the errors remain basically unchanged except for channels 4 and M3 which required large tuning coefficients. In these channels, significant improvements in the standard deviation occured as well. The tuning coefficient in channel 7 appears to be somewhat too large when judged against the whole set. With the exception of the stratospheric sounding channel 2, the standard deviation of the tuned 15 μm and 4.3μm brightness temperatures in channels used for retrievals of temperature profiles are of the order of .7°. This variance in the agreement of computed and observed brightness temperatures is comparable with the criterion used for the convergence of the physically-derived temperature profiles. Agreement in channel 7, used only for cloud height determination, is somewhat worse, possibly because of the effects of incorrect surface temperature. We believe the agreement in the microwave channels, which is poorer than the infra-red channels by about 50%, is the result of poorer colocations with the lower spatial resolution microwave observations. The eighth column of Table 1.2 shows the standard deviations of the measurements for each channel. The ratio of the standard deviation of the observations to the standard deviation of the errors, which is significant for all but channel 1, may be thought of as a signal to noise ratio for each channel. The last column shows the standard deviations of the computed brightness temperatures using the tuned transmittances. The computed brightness temperatures show basically the same variances as the observations.

Cloudy Cases

Table 1.3 gives similar statistics for cases in the Jan-Feb 1979 period in which both fields of view were found to be partially cloud covered, that is, $\eta > 0$. In this case, brightness temperatures computed from the radiosonde pro-

file were compared to brightness temperature reconstructed from the satellite observations using equations (1.10) and (1.11). To avoid highly overcast situation, only cases with $\eta \leq 2$ were included in the statistics. Because η is determined by channel 13, radiances in this channel give "perfect agreement". No cloud correction is made to the microwave observations. As in Table 1.2, statistics for the window channels are given for the night cases only.

All computations were done using transmittances tuned with the coefficients determined from the subset of clear observations occuring in the first two weeks of January. These coefficients are shown in column 2. The next two columns show the mean and standard deviation of the difference between computed and reconstructed brightness temperatures. The fifth column gives the root mean square of the difference between the reconstructed brightness temperature and the brightness temperature observed in field of view 1. For the channels sounding beneath the cloud layer, this difference is a measure of the cloud correction applied to the radiances. For channels sounding above the clouds, the difference between the observations in both fields of view is assumed to be noise. In these channels, nominally 1-3, the clear column radiance is taken as the average of the radiances in both fields of view, using an effective η of -.5. The difference between reconstructed and observed radiances is then a measure of instrumental noise in these channels. As in Table 1.2, the last two columns show the standard deviation of the reconstructed clear column and computed brightness temperatures.

The bias errors shown in Table 1.3 are all small and comparable to those found in the clear cases. The tuning coefficients determined from clear cases are therefore applicable to cloudy cases as well. The standard deviation of the errors average .25° C larger than those in clear cases. The increase in error is small compared to the cloud corrections made, however, and indi-

TABLE 1.3

COMPARISON OF RECONSTRUCTED AND COMPUTED BRIGHTNESS TEMPERATURES (°C)

CLOUDY CASES JAN - FEB 1979 (146 CASES)

CH	ε (a)	MEAN (COMP-RECON)	STD DEV	RMS RECON-OBS	STD DEV RECON	STD DEV COMP
1	0	.87	2.60	1.34	3.99	4.46
*2	0	-.40	1.31	.38	5.13	5.06
3	0	.91	1.46	.29	5.02	4.40
*4	.12	-.02	1.11	1.11	3.21	3.27
5	.03	.02	1.38	2.55	4.83	4.97
6	.015	-.23	1.64	3.86	5.89	6.08
7	.04	-.08	1.85	5.11	5.83	5.78
**8	0	.42	1.19	5.76	7.01	6.68
*13(c)	0	0	0	3.90	8.09	8.09
*14	.04	-.02	.60	3.17	8.19	8.50
*15	.035	-.04	1.05	2.29	6.83	7.19
16	0	.14	2.51	.65	3.36	4.03
**18	0	.22	1.18	3.54	9.44	8.97
**19	0	.23	1.25	3.33	8.91	8.39
M1(b)	0	0	0	0	10.75	10.75
*M2	.035	-.07	.85	0	7.60	7.42
*M3	.10	-.17	.98	0	4.56	4.30
*M4	0	-.43	1.43	0	8.50	7.86

a - ε determined from 20 clear Jan cases
b - used to determine ε emissivity
c - used to determine η
* - used for temperature sounding
** - 64 night cases only

cate that infra-red observations can be used in partially cloudy areas. The degradation in accuracy is somewhat worse in channels 5, 6, and 7 which are not used in temperature sounding. The agreement in the window channels, which is in part determined by the accuracy of the climatological sea surface temperatures, is not degraded under partially cloudy conditions.

Tables 1.4 and 1.5 are equivalent to Tables 1.2 and 1.3 for cases taken from May 1979. The average absolute value of the bias in the untuned case is .73° C and the average of the standard deviation is .96° C. In both sets, the tuning coefficients obtained from the clear cases in the first two weeks of January were used in the calculations. The untuned biases shown in Table 1.4 are very similar to those in Table 1.2 for those channels not sensitive to the stratosphere or surface temperature. Consequently, the transmittances tuned with the set of winter tuning coefficients produce only small residual biases in the computed brightness temperatures. Tuning of channel 4 and M3 again decreased the standard deviation of the errors as well as removing the biases. As in the winter case, it appears that the tuning coefficient for channel 7 is somewhat too large. The standard deviations of the errors in the spring cases are similar to those found in the winter. Channels 2, 3, and M4, sounding the mid-lower stratosphere, all appear to have a significantly colder bias in the spring than in the winter. This may be reflective of errors in the spring climatology used in extrapolating the radiosonde profiles above their highest reported level. The NMC stratospheric analysis was not available for use with the spring cases. The results in Table 1.5, showing statistics for cloudy cases from the spring period, are likewise very similar to those of Table 1.3. The average standard deviation of the errors is .3° higher in the May cloudy cases than in the May clear cases, but as in the winter, the largest increases in error occur in channels not used in the GIAS temperature retrievals. As in Table 1.4, the

TABLE 1.4

COMPARISON OF OBSERVED AND COMPUTED BRIGHTNESS TEMPERATURE (°C)

CLEAR CASES MAY 5 - MAY 20 1979 (33 CASES)

CH	UNTUNED		TUNED			STD DEV	STD DEV
	MEAN COMP-OBS	STD DEV	ε(a)	MEAN	STD DEV	OBS	COMP
1	1.55	2.00	0	1.55	2.00	2.57	2.72
*2	-1.55	1.14	0	-1.55	1.14	2.97	3.10
3	.64	1.00	0	.64	1.00	2.46	2.36
*4	1.62	.72	.12	-.27	.67	2.20	2.32
5	.54	.67	.03	-.10	.67	3.58	3.61
6	.18	.81	.015	-.25	.81	4.24	4.28
7	.32	1.02	.04	-.37	1.02	4.14	3.96
**8	-.54	1.18	0	-.54	1.18	3.83	3.54
13	-.14	.92	0	-.14	.92	5.67	5.33
14	.72	.66	.04	-.09	.67	5.79	5.70
15	.80	.62	—.035	-.02	.64	4.98	4.95
16	.87	1.84	0	.87	1.84	1.97	2.67
**18	-.39	.56	0	-.09	.56	4.87	4.81
**19	-.38	.61	0	-.02	.61	4.50	4.45
M1	0	0(b)	0	0	0	8.91	8.91
*M2	.30	.72	.035	-.44	.71	5.89	5.69
*M3	1.32	.91	.10	-.22	.79	3.65	3.66
*M4	-.61	.97	0	-.61	.97	4.53	4.39

a - ε determined from 20 clear Jan. cases
b - used to determine emissivity
* - used for temperature sounding
** - 19 night cases only

TABLE 1.5

COMPARISON OF RECONSTRUCTED AND COMPUTED BRIGHTNESS TEMPERATURES (°C)

CLOUDY CASES MAY 5 - MAY 20 1979 (47 CASES)

CH	ε(a)	MEAN (COMP-OBS)	STD DEV	RMS RECON-OBS	STD DEV RECON	STD DEV COMP
1	0	1.66	2.08	1.42	3.68	3.42
*2	0	-.84	1.28	.38	4.01	4.16
3	0	.30	1.38	.30	4.35	3.69
*4	.12	-.09	1.04	.73	1.96	1.77
5	.03	.09	1.50	1.67	3.81	3.81
6	.015	-.31	1.73	2.63	5.31	5.43
7	.04	-.32	1.84	3.79	5.43	5.63
**8	0	.31	.83	5.18	6.12	6.24
*13(c)	0	0	0	2.01	7.60	7.60
*14	.04	.01	.51	1.37	7.42	7.53
*15	.035	.34	1.05	.43	5.83	5.76
16	0	-.57	1.81	.08	2.22	1.80
**18	0	-.35	.72	3.42	7.64	7.57
**19	0	-.72	1.31	3.29	7.42	7.53
M1(b)	0	0	0	0	11.53	11.53
*M2	.035	.06	.70	0	6.10	5.89
*M3	.10	-.36	.84	0	3.80	3.51
*M4	0	-.83	1.23	0	6.82	6.39

a - ε determined from 20 clear Jan. cases
b - used to determine emissivity
c - used to determine η
* - used for temperature sounding
** - 18 night cases only

biases for channels 2, 3, and M4 are again significantly lower than in the winter period.

1.7. Summary

Tables 1.2-1.5 show that under clear conditions, given the temperature-humidity profile, radiances can be calculated which agree with observations to about .7°C for the HIRS2 channels not sensitive to the upper stratosphere or the surface, and about 1°C for the MSU channels. Part of these differences are due to noise and sampling differences in space and time between the satellite and radiosonde. The accuracy of this calculation is sufficient to allow for determination of atmospheric temperature profiles via an iterative physical technique in which temperature profiles are found, which when substituted in the radiative transfer, match the observations to a desired accuracy. Under partially cloudy conditions, cloud corrections can be made to the infra-red observations to still allow for accurate temperature soundings.

Significant bias errors exist in the calculations for some channels, however. These errors can be removed to a large extent by an empirical tuning of the transmittance functions with coefficients which appear to be transferable from one season to another. In all cases, additional atmospheric attenuation appears necessary in the calculated transmittance functions.

While empirical tuning coefficients are sufficient for practical use, it is much more desirable to directly eliminate that portion of the bias that results from theoretical uncertainties. Coffee and Goldman (1981) have indicated that atmospheric absorption due to the ν_2 band of HCN, centered at 712 cm^{-1}, is significant in that spectral region. Absorption by HCN was not included in the line by line calculations done in this work. In addition, a more accurate value of .31 ppmv for the tropospheric mixing ratio of N_2O [Chedin, 1982], rather than the value of .28 ppmv, reported in McClatchey et

al. [1973] should be used in the calculations. We are currently including HCN absorption in our calculation as well as modifying the N_2O mixing ratio to see the extent to which these factors may explain the untuned biases in HIRS channels 3-5, and 14-15.

The rapid transmittance algorithm used in the calculations in described in the next chapter. It will be shown to contribute only small errors to the radiance calculations as compared to calculations based on line-by-line computed transmittance functions.

Chapter 2

A Rapid Algorithm for Modeling Atmospheric Transmittances

2.1 The physical basis for the form of the rapid algorithm

The rapid transmittance algorithm is of the form of equation 1.7. The averaged discrete line transmittance through the atmosphere from pressure P_ℓ to the top of the atmosphere, at a zenith θ, as seen by channel i, is modelled as

$$\bar{\tau}_{iL}(P_\ell,\theta) = \prod_{j=1}^{\ell} \bar{\tau}_{iF}(P_j,P_{j-1},\theta)\ \bar{\tau}_{iO}(P_j,P_{j-1},\theta)\ \bar{\tau}_{iW}(P_j,P_{j-1},\theta \qquad (2.1)$$

where $\bar{\tau}_{iF}$, $\bar{\tau}_{iO}$, and $\bar{\tau}_{iW}$ represent models for effective layer transmittances from pressure P_j to P_{j-1} ($P_j > P_{j-1}$) at zenith angle θ. The term $\bar{\tau}_{iF}$ represents absorption by gases assumed to have a fixed mixing ratio, while $\bar{\tau}_{iO}$ and $\bar{\tau}_{iW}$ represent absorption due to ozone and water vapor respectively. $\bar{\tau}_{iL}(P_\ell,\theta)$ from equation (2.1) is used to model $\tau_{iL}(P,\theta)$ from equation 1.2.

Line-by-line calculations done at zenith angles of 0°, 50°, and 70°, for eight climatological profiles shown in Table 2.1-2.3 are used to generate the coefficients for the effective transmittance models at the appropriate angle. Effective layer transmittances at other zenith angles are obtained by linear interpolation of the logarithm of the effective layer transmittance in sec θ. $\bar{\tau}_{iL}(P_\ell,\theta)$ computed from equation 2.1 is then multiplied by additional factors to account for H_2O continuum absorpton, N_2 continuum absorption, and scattering as discussed in the text.

Because channel i is not monochromatic, the effective layer transmittances do not obey the properties of equation 1.4. Instead, given line by line transmittance calculations for $\tau_{iF}(P,\theta)$, $\tau_{iFO}(P,\theta)$, and $\tau_{iFOW}(P,\theta)$, corresponding respectively to absorption using only gases of fixed distribution, using fixed gases and ozone, and using all species, we define effective mean layer transmittances

TABLE 2.1

CLIMATOLOGICAL TEMPERATURE PROFILES (°C)

P(MB)	JAN 0°N	JAN 20°N	JAN 40°N	JAN 50°N	JAN 70°N	JUL 20°N	JUL 40°N	JUL 60°N	STD. PRO.
1	270.0	270.0	265.0	250.0	235.0	270.0	285.0	290.0	265.0
2	263.4	263.7	259.0	245.8	231.2	264.1	277.5	282.4	259.7
5	241.4	242.7	239.0	231.8	218.2	244.6	252.5	257.3	242.2
10	227.0	229.0	225.9	222.6	210.6	231.9	236.1	240.9	230.8
20	222.0	222.5	219.7	217.7	206.5	226.5	229.5	232.5	224.5
30	217.5	219.5	217.5	217.2	206.0	222.5	222.5	229.5	221.0
50	207.0	211.1	214.9	217.0	206.8	213.7	219.1	226.8	213.5
70	196.6	201.3	214.1	217.4	208.5	206.6	214.9	226.1	208.1
100	193.7	198.1	214.0	218.8	211.6	200.3	212.3	225.6	206.1
150	204.0	208.1	217.5	220.2	213.4	207.1	215.6	226.4	211.0
200	217.8	218.1	217.9	218.2	214.7	218.9	221.5	224.4	216.9
250	234.3	227.4	221.7	220.7	215.0	229.7	229.2	227.4	224.6
300	240.0	236.4	225.8	221.6	215.2	239.9	237.8	230.8	232.1
400	255.3	251.3	238.1	232.7	225.9	245.9	252.0	244.0	247.3
500	266.7	262.7	248.1	241.9	235.0	266.2	262.9	254.8	259.0
700	282.2	279.1	264.6	247.6	249.2	282.9	279.5	270.7	275.9
850	289.5	285.5	270.8	262.8	255.4	291.6	288.3	279.3	284.2
1000	295.5	292.5	277.7	270.1	265.8	297.8	292.0	284.5	290.0

TABLE 2.2

CLIMATOLOGICAL OZONE PROFILES (PPMV)

P(MB)	JAN 0°N ρ	JAN 20°N ρ	JAN 40°N ρ	JAN 50°N ρ	JAN 70°N ρ	JUL 20°N ρ	JUL 40°N ρ	JUL 60°N ρ
1	3.818	3.812	2.661	2.023	1.342	3.805	2.352	1.547
2	3.818	3.812	2.661	2.023	1.342	3.805	2.352	1.547
5	4.583	4.558	3.395	2.657	1.744	4.348	3.067	2.020
10	6.876	6.790	5.599	4.559	2.952	5.978	5.211	3.439
20	7.808	7.778	6.903	5.517	3.889	6.542	6.180	3.979
30	7.119	7.209	6.446	5.496	4.084	5.978	5.322	3.866
50	2.989	3.774	4.438	4.711	4.318	3.080	3.291	3.140
70	.634	1.449	2.446	3.351	3.623	1.419	2.023	2.597
100	.242	.513	1.147	2.144	2.838	.604	1.087	1.932
150	.085	.154	.664	1.208	1.902	.205	.483	1.177
200	.042	.063	.332	.694	1.178	.094	.272	.694
250	.034	.053	.168	.400	.641	.071	.193	.398
300	.031	.046	.145	.254	.374	.064	.145	.253
400	.030	.038	.101	.145	.189	.057	.104	.151
500	.030	.029	.062	.072	.083	.051	.071	.091
700	.021	.020	.033	.032	.026	.039	.050	.047
850	.018	.018	.025	.025	.024	.031	.048	.037
1000	.018	.018	.024	.024	.024	.026	.044	.036
Total 0_3 (cm atm)	.244	.282	.355	.430	.480	.263	.307	.362

TABLE 2.3

CLIMATOLOGICAL WATER VAPOR PROFILES ($gm/cm^2 atm$)

P(MB)	JAN 0°N ρ	JAN 20°N ρ	JAN 40°N ρ	JAN 50°N ρ	JAN 70°N ρ	JUL 20°N ρ	JUL 40°N ρ	JUL 60°N ρ
1	.002	.002	.002	.002	.002	.002	.002	.002
2	.002	.002	.002	.002	.002	.002	.002	.002
5	.002	.002	.002	.002	.002	.002	.002	.002
10	.002	.002	.002	.002	.002	.002	.002	.002
20	.002	.002	.002	.002	.002	.002	.002	.002
30	.002	.002	.002	.002	.002	.002	.002	.002
50	.002	.002	.002	.002	.003	.002	.002	.002
70	.002	.002	.002	.003	.006	.002	.002	.002
100	.002	.002	.002	.007	.010	.002	.002	.002
150	.006	.005	.005	.016	.017	.006	.006	.002
200	.027	.018	.013	.032	.029	.028	.023	.002
250	.11	.06	.05	.07	.04	.12	.09	.01
300	.21	.11	.06	.09	.06	.23	.16	.03
400	.59	.25	.13	.15	.08	.65	.43	.18
500	1.48	.66	.36	.26	.15	1.68	1.12	.71
700	4.01	2.53	1.28	.84	.43	4.92	3.60	2.55
850	8.27	5.95	2.63	1.70	.76	9.81	7.09	4.85
1000	12.38	9.25	3.95	2.31	.82	14.42	10.72	6.84
Total H_2O gm/cm^2	3.64	2.53	1.14	0.73	0.32	4.31	3.14	2.08

$$\tau_{i}(P_j,P_{j-1},\theta) \equiv \tau(P_j,\theta)/\tau_{i}(P_{j-1},\theta), \tag{2.2}$$

$$\tau_{iO}(P_j,P_{j-1},\theta) \equiv \frac{\tau_{iFO}(P_j,P_{j-1},\theta)}{\tau_{iF}(P_j,P_{j-1},\theta)} \tag{2.3}$$

and

$$\tau_{iW}(P_j,P_{j-1},\theta) \equiv \frac{\tau_{iFOW}(P_j,P_{j-1},\theta)}{\tau_{iFO}(P_j,P_{j-1},\theta)} \tag{2.4}$$

Equation 2.2 defines an effective mean layer transmittance based on line-by-line calculations using any combination of constituents [Halem and Susskind, 1977]. Note that the effective layer transmittances for ozone (equation A3) and water vapor (equation 2.4) do not involve in any way calculations based on absorption of water vapor or ozone alone [Susskind, 1975]. In fact, significant differences may exist between effective layer transmittances defined from equations 2.3, 2.4 and those defined in equation 2.2 based on the single species transmittances. Table A2 of Halem and Susskind [1977] shows that the brightness temperatures computed for VTPR channel 7 using line-by-line transmittances, $\tau_{FO}\tau_{W}$, differ from those computed using line-by-line τ_{FOW}, by .4°C for a tropical temperature humidity profile. The spectral response of VTPR channel 7 is very similar to that of HIRS channel 7. Errors of similar magnitude are then expected for HIRS2 channel 7.

2.2 The model for water vapor and ozone absorption

The basic assumption of the models of water vapor and ozone transmittance is that the effective mean layer transmittances in eqs. (2.3, 2.4) can be treated as having the transmittance properties of a gas in a homogeneous layer having the mean temperature T, and pressure P, of the atmospheric layer, and vertical column density u of the absorbing gas in the layer. This assumption is reason-

ably valid because use of equation 2.2 removes most of the dependance of the mean layer transmittance on the properties of the atmosphere above the layer, and absorption due to water vapor and ozone has a second order effect on the radiances in the temperature sounding channels. We then expect the log of the mean layer transmittance to be proportional to u for weakly absorbing lines, and $u^{1/2}$ for strong lines. For a composite of lines, an effective exponent of intermediate value is obtained. The absorption coefficient depends on the pressure P and the temperature T.

The following form was therefore used to model the effective water and ozone transmittances for all channels and all layers:

$$\bar{\tau}_{ic}(P_j,P_{j-1},\theta) = \exp- \; A_{i,j,c}(\theta)[1 - B_{i,c}(T_j-273)] \; u_c(j,j-1)^{N_{i,c}} \qquad (2.5)$$

where c stands for constituent, either ozone or water vapor, $u_c(j,j-1)$ is the integrated column density of the species in the layer between j and j-1, $N_{i,c}$ is a channel and species dependent constant between .5 and 1, $A_{i,j,c}$ is an effective channel, species, pressure, and angle dependent absorption coefficient, and $B_{i,c}$ is a channel and species dependent constant (per-cent change per degree). For simplicity, the temperature dependance, $B_{i,c}$, and exponent, $N_{i,c}$, are taken to be independent of pressure and angle. The coefficients A, B, and N are determined from the effective mean layer transmittances computed from the line-by-line calculations from the eight climatological profiles shown in Tables 2.1-2.3. Table 2.4 shows select values of the coefficients for the water vapor and ozone models. $A(P,\theta)$ is raised to the power 1/N so as to be in units of $(mol/cm^{-2})^{-1}$. The absorption coefficients are shown at 1000 mb and 100 mb respectively, where absorption due to water vapor and ozone is most significant. Because of the complex nature of the effective transmittance, the pressure behavior of A is not simple. The range of coefficients for a particular channel in the pressure region where significant absorption is present

TABLE 2.4

SELECT WATER VAPOR AND OZONE TRANSMITTANCE COEFFICIENTS

	WATER VAPOR			OZONE		
CHANNEL	$A(1000,0)^{1/N}$ $(MOL^{-1}CM^2)$	B	N	$A(100,0)^{1/N}$ $(MOL^{-1}CM^2)$	B	N
1	0	0	1.0	0	0	1
2	0	0	1.0	6.2 E-23	0	1
3	0	0	1.0	2.6 E-21	0	.9
4	1.6 E-24	0	.8	3.6 E-22	0	.7
5	4.2 E-25	0	.85	1.9 E-21	0	.8
6	8.4 E-24	0	.65	5.1 E-21	0	1
7	4.4 E-26	.016	.5	3.1 E-21	0	1
8	4.5 E-25	0	.9	0	0	1
9	6.9 E-25	0	1.	7.8 E-20	0	.95
10	1.1 E-24	0	.8	0	0	1
11	5.1 E-23	0	.7	0	0	1
12	4.2 E-22	0	.6	0	0	1
13	1.4 E-24	0	1.0	0	0	1
14	2.8 E-25	.019	.8	0	0	1
15	6.8 E-25	.017	.95	0	0	1
16	1.4 E-24	0	1.0	0	0	1
18	6.7 E-26	.016	1.0	0	0	1
19	3.9 E-25	0	.8	0	0	1
M1	1.1 E-24	0	1.0	0	0	1
M2	1.2 E-24	0	1.0	0	0	1
M3	1.3 E-24	0	1.0	0	0	1
M4	1.4 E-24	0	1.0	0	0	1

is generally less than 20%. For most channels, B is found to be nearly zero and N is nearly 1.

McMillin et al., (1979), and Weinreb and Neuendorfer (1973) have given more elaborate models to account for the effects of water vapor on atmospheric transmittances. In both cases, the coefficients for the models are based on calculations of averaged transmittances due to water vapor alone. These modeled transmittances are multiplied by the dry transmittances to give total transmittances as in equation 2.1. The appropriate quantities to use are the effective mean layer transmittances as defined in equation 2.4, which differs significantly from the mean layer transmittances computed from the absorbing gas alone, because absorption by a gas such as H_2O is not totally uncorrelated with absorption by the fixed gases, especially in a relatively narrow channel, where only one or two H_2O lines may be of significance.

2.3 The model for absorption due to gases of fixed distribution

Most of the absorption for the temperature sounding channels is due to the gases of fixed distribution, primarily CO_2 and N_2O. The transmittance at a given angle depends only on the temperature profile. The effective mean layer transmittance for each reference angle is modelled according to

$$\tau_{iF}(P_j, P_{j-1}, \theta) = A_{ij}(\theta) + B_{ij}(\theta)(T_j - T_j^o) + C_{ij}(\theta)(\tilde{T}_{ij}(\theta) - \tilde{T}_{ij}^o(\theta)) \qquad (2.6)$$

where T_j is the mean temperature in the layer j, between P_j to P_{j-1}, for the temperature profile under consideration, T_j^o is the mean temperature in layer j in a standard temperature profile shown in Table A1, and $\tilde{T}_{ij}$ and $\tilde{T}_{ij}^o$ are effective mean temperatures for the entire profile from P_j to the top of the atmosphere for the temperature profile under consideration and the standard temperature profile respectively. The effective mean temperature above pressure P for channel i is defined as the average temperature above pressure P

weighted by the weighting function for channel i. The effective temperature is then channel and angle dependent and is defined as

$$\tilde{T}_{ij}(\theta) \equiv \frac{1}{1-\tau_i^o(P_j,\theta)} \int_o^{P_j} T(P)\, \frac{d\tau_i(\theta)}{dP}\, dP \qquad (2.7)$$

where $\tau_i^o(P,\theta)$ is the transmittance of channel i for the standard temperature profile.

The coefficients $A_{ij}(\theta)$, $B_i(\theta)$, and $C_{ij}(\theta)$ are determined so as to give the best fit in the least squares sense to the values of τ_{iF} obtained from line-by-line calculations. As expected, the coefficient $A_{ij}(\theta)$ was found to be very close to $\tau_{iF}^o(P_j,P_{j-1},\theta)$, the effective layer transmittances for the standard profile shown in Table 2.1.

The algorithm is essentially equivalent to that of McMillin and Fleming (1978), except that McMillin and Fleming expand the effective layer transmittances in a four term expansion about a standard profile effective layer transmittance. Two of their terms deal with the temperature in the layer and the remaining two contain channel independent weighted temperatures above the layer.

2.4 Ability of the model to fit the climatological profiles

The importance of the transmittance error is the error made in computing brightness temperature, or equivalent black body temperature, which arises from using incorrect transmittances in equation 1 of the text. Table 2.5 shows the ability of the rapid algorithm to reproduce the brightness temperatures for the profiles used to generate the coefficients. The second and third columns of Table 2.5 summarize the maximum and RMS errors in brightness temperatures for the eight profiles computed using the transmittance functions from equation 2.6 and the coefficients determined from the fit as compared to those computed using τ_F, the line-by-line transmittance. In computing these brightness tempera-

TABLE 2.5

TRANSMITTANCE MODEL BRIGHTNESS TEMPERATURE ERRORS(°C)FOR HIRS CHANNELS AT NADIR VIEWING

CHANNEL	MODEL ERRORS FIXED GAS		MODEL ERRORS FIXED+OZONE		MODEL ERRORS FIXED+OZONE+WATER		MAXIMUM EFFECT OZONE	WATER	OZONE+WATER +CONTINUUM
	MAX	RMS	MAX	RMS	MAX	RMS			
1	.038	.021	.038	.021	.038	.021	0	0	0
2	.085	.055	.085	.055	.085	.055	0	0	0
3	.015	.009	.013	.006	.013	.006	.27	0	.27
4	.071	.041	.079	.048	.077	.050	.81	.47	1.13
5	.144	.074	.129	.079	.145	.082	2.04	1.08	2.90
6	.092	.049	.076	.047	.105	.063	1.58	1.92	4.57
7	.153	.086	.119	.077	.115	.079	1.10	3.33	5.80
8	.002	.001	.002	.001	.103	.063	0	1.33	4.89
9	.008	.003	1.535	.922	1.464	.891	26.81	.70	27.48
10	.003	.002	.003	.002	.264	.122	0	6.26	7.71
11	.005	.003	.005	.003	1.108	.605	0	33.23	33.23
12	.000	.000	.000	.000	1.793	.982	0	57.57	57.57
13	.014	.007	.014	.007	.073	.038	0	1.14	1.18
14	.027	.012	.027	.012	.028	.014	0	.57	.58
15	.033	.014	.033	.014	.033	.013	0	.30	.31
16	.085	.039	.085	.039	.085	.041	0	.06	.06
18	.003	.001	.003	.001	.003	.001	0	.08	.10
19	.001	.000	.001	.000	.050	.039	0	1.71	1.73

tures, it was assumed that the surface was a black body whose temperature was equal to the 1000 mb air temperature. The maximum difference in brightness temperature arising from use of the modelled transmittances rather than the exact transmittances is equal to .15°C and is on the order of the instrumental noise. The next four columns indicate maximum and RMS errors for the brightness temperatures computed for the eight profiles using τ_{FO} compared to $\overline{\tau}_F\ \overline{\tau}_O$ and τ_{FOW} compared to $\overline{\tau}_F\ \overline{\tau}_O\ \overline{\tau}_W$. The exact temperature-humidity-ozone profiles were used in the calculations.

The last three columns show the extent to which absorption due to O_3 and water vapor effects the brightness temperatures of each channel. The column marked maximum O_3 effect gives the maximum difference of brightness temperature, computed, on the one hand, using line by line transmittances calculated with only the fixed gases, τ_F, and, on the other hand, using line-by-line transmittances calculated also including O_3 absorption, τ_{FO}. The column marked maximum H_2O effect gives the brightness temperature difference computed using τ_{FO} on the one hand, and τ_{FOW}, the transmittances including all species, on the other. The maximum total effect, including absorption due to ozone and water vapor lines and water continuum, is shown in the last column.

Except for channels 8-12, which are sensitive primarily to absorption of H_2O or O_3 themselves, the transmittance model fits the eight climatological profiles extremely well, the largest source of error coming from the fixed gas model. In channels, 9, 11, and 12, where the effects of absorption due to O_3 and H_2O are the order of 20-55°C, the rapid algorithm errors are larger than 1°C and a more elaborate algorithm appears to be necessary to reduce the errors. Inclusion of a term representative of the effective species column density above the layer, analogous to the third term in equation 2.6, as well as allowing for a

pressure dependance of N, should achieve more accurate results.

2.5 Test of the model on independent profiles

Line-by-line calculations were run for 2 of the 72 clear profiles from the January - February period, to assess the contribution of the rapid transmittance algorithm as a source of error in the radiance calculations for real profiles. The first was a mid-latitude profile chosen because the temperature profile differed significantly from the climatological set used to generate the rapid algorithm coefficients. The second profile was a very humid tropical profile observed at a large zenith angle. This was chosen to test the water vapor correction model in an extreme case. The two profiles are shown in Table 2.6. The radiosonde temperature profiles were reported to 10 mb and 20 mb respectively. The humidity profiles were reported to 400 and 300 mb. Values extrapolated from the radiosonde reports are marked by *. Climatological values, marked by **, were used for the sea surface temperature, and the 0_3 profile, the 1 mb temperature temperature, and humidities above 100 mb.

Table 2.7 shows for each profile, T_{OBS}, the observed brightness temperatures for each channel, the difference between T_{OBS} and T_M, the brightness temperatures computed using equation 1.1 and the untuned rapid algorithm model generated transmittance coefficients, and the differences between T_M and T_L, the brightness temperatures computed using line-by-line generated transmittances. The calculations are all run at the appropriate zenith angles, 22.8° for the mid-latitude profile and 46.9° for the tropical profile. Thus, all aspects of the rapid algorithm, including zenith angle interpolation, are tested simultaneously by this comparison.

The brightness temperature errors introduced by the rapid algorithm, shown in the columns T_M-T_L, are of the order of .1°C for all channels but those primarily sensitive to water vapor or ozone themselves. The errors are similar to

TABLE 2.6

ATMOSPHERIC SOUNDINGS USED TO TEST THE RAPID TRANSMITTANCE ALGORITHM

MID LATITUDE PROFILE
FEB 9 0Z 47°N, 17°W
ZENITH ANGLE = 22.8°
SURFACE PRESSURE = 992 MB
SST = **284.7°K PREC. WAT. = 1.66 gm/cm^2
O_3 PROFILES = **JAN 50°N

TROPICAL PROFILE
JAN 5 0Z 14°S, 171°W
ZENITH ANGLE = 46.9°
SURFACE PRESSURE = 1009 MB
SST = **302.1°K PREC. WAT. = 6.56 gm/cm
OZONE PROFILE = **JAN 0°N

P(MB)	T(°K)	q(gm/cm^{2}atm)	T°(K)	q(gm/cm^{2}atm)
1	**259.1	**.002	**274.2	**.002
2	*245.6	**.002	*258.2	**.002
5	*227.6	**.002	*240.6	**.002
10	208.7	**.002	*232.9	**.002
20	206.1	**.002	225.7	**.002
30	209.7	**.002	221.7	**.002
50	215.1	**.002	205.9	**.002
70	218.5	**.002	200.5	**.002
100	222.1	**.002	191.7	**.002
150	222.3	*.005	207.7	*.02
200	224.7	*.02	221.5	*.09
250	222.9	*.04	234.3	*.28
300	218.1	*.08	244.5	.76
400	235.5	.24	259.5	2.0
500	248.1	.85	269.7	3.9
700	267.3	2.5	283.2	8.2
850	277.0	4.7	291.4	16.3
SURFACE	285.4	*6.6	300.2	21.0

**CLIMATOLOGY
*EXTRAPOLATED

TABLE 2.7

ASSESSMENT OF ERRORS CAUSED BY RAPID ALGORITHM (°C)

	MID LATITUDE PROFILE			TROPICAL PROFILE		
CHANNEL	T_{OBS}*	$T_M - T_{OBS}$	$T_M - T_L$	T_{OBS}	$T_M - T_{OBS}$	
1	225.74	-.16	-.03	234.28	2.48	-.10
2	217.48	.43	.06	218.15	1.21	-.13
3	219.22	.59	.08	216.69	2.95	.10
4	226.29	1.28	-.04	227.56	3.32	.03
5	238.63	.71	-.08	243.85	1.25	.02
6	250.23	.13	-.12	255.02	.90	-.02
7	262.25	.51	-.02	265.89	1.20	.07
8	282.75	-.66	-.10	289.85	-.56	-.68
9	251.79	2.44	-.85	272.53	-2.96	-1.43
10	278.81	-.75	-.03	284.67	-1.20	-.81
11	255.86	-5.64	-.20	253.64	-1.53	-.99
12	242.30	-10.30	.02	241.31	-5.96	.50
13	268.49	-.30	.02	278.47	-.11	-.12
14	256.56	1.03	.05	265.67	1.38	.10
15	243.84	1.17	.08	251.82	1.41	.06
16	225.82	1.25	.10	231.44	1.58	.16
18	282.93	-1.21	.00	299.79*	-1.76	.01
19	284.48	-2.25	.03	301.71*	-4.96	-.16
M1	219.98	0**	-.02	253.41	0**	.04
M2	245.33	-.26	.01	252.26	.87	.08
M3	226.44	.19	.01	221.64	1.62	.01
M4	217.08	.24	-.06	205.38	1.95	-.06

*DAYTIME CASE
**USED TO COMPUTE EMISSIVITY

those found in Table 2.5 representing the quality of fit to the eight climatological profiles.

The large differences in observed and computed brightness tempertures for channels 11 and 12 in the mid-latitude profile, and channel 12 in the tropical profile, are most likely the result of errors in the extrapolation above the incomplete water vapor profiles. The climatological O_3 profiles did reasonably well in accounting for observations in channel 9. The errors introduced in the brightness temperature by the rapid algorithm transmittance model are insignificant except for those channels whose absorption is due primarily to water vapor and ozone. These channels have not yet been introduced in the GLAS processing scheme. When they are introduced in the near future, the model for these channels may have to be improved.

Chapter 3

Theory and Application of the Glas Physical Inversion Method

3.1 Overview of the GLAS Physical Inversion Method

The GLAS physical inversion approach to temperature sounding from satellite observations is fundamentally different from the statistical regression method used operationally at NOAA/NESS in that heavy reliance is placed on the ability to model accurately the instrumental response to atmospheric and surface conditions, while no use is made of statistical relationships between satellite observations and atmospheric temperature profiles. The method involves starting with a guess set of atmospheric and surface conditions from which expected brightness temperatures for the satellite observations are computed. Then, iterative relaxation of atmospheric and surface conditions is performed according to the difference between observed and computed brightness temperatures until sufficient agreement is reached. If sufficient agreement can not be obtained, no retrieval is produced for that location.

The basic advantages of the method arise from the ability to utilize first guess and other a-priori information to account directly for all factors affecting the observations, and to determine areas where retrievals should be rejected. In addition, GLAS retrievals can be derived in regions of high topography, where operational retrievals were not processed during FGGE. Most important of all, a complete set of auxilliary meteorological parameters can be simultaneously determined which are all compatible with each other and the observations.

The GLAS processing scheme is comprised sequentially of the following elements:

1. Calibration of the data.
2. Averaging of the data into fields of view.
3. Attaching initial guess conditions, $T^O(P)$, $q^O(P)$, P_s.
4. Computation of clear-column radiances R_i^O, from the initial guess conditions.
5. Determination of the surface emissivity at 50.3 GHz, ε^N, to compute microwave radiances.
6. Determination of $\tilde{R}_i^N$, the iterative reconstructed clear-column infrared radiances from potentially cloud-contaminated radiance observations, $\tilde{R}_i$. When it is determined to be too cloudy for reconstruction of clear column radiances, no retrieval is performed and steps 7-10 are skipped.
7. Determination of T_s^N, the iterative sea/land surface temperature.
8. Calculation of R_i^N, the clear-column radiances using the iterative sea/land surface temperature and temperature profile.
9. Comparison of $\tilde{R}_i^N$ and R_i^N for the temperature sounding channels.
10. If sufficient agreement between $\tilde{R}_i^N$ and R_i^N is not found in step 9, calculation of $T^{N+1}(P)$, the next (iterative) temperature profile, and return to step 5 to compute ε^{N+1} and continue the iterative procedure. Otherwise, the iterative procedure is terminated.
11. Set quality flags.
12. Calculation of cloud field parameters under all conditions.

3.2 Preparation of the Satellite Data for Analysis

The HIRS2 and MSU data used by GLAS is the level I-B data obtained from NOAA/EDIS. Uncalibrated observations are given for each channel at each spot observed by the instrument, which is earth located and flagged. Calibration coefficients are provided with the data. The data is calibrated at GLAS using the coefficients with the appropriate algorithm described by Lauritson et al. [1979].

Figure (1) shows the scan patterns of HIRS2 and MSU. In the processing system used in analysis of the data, one sounding, representative of an area of 125 x 125 km, was performed at a spacing of roughly 250 x 250 km. This resolution and spacing was chosen so as to be comparable to that used for operational temperature sounding by NOAA/NESS. Observations at the 125 x 125 km resolution were generated by averaging of the HIRS2 data as shown in the figure. First the HIRS spots are blocked into roughly 250 x 250 km areas in groups of 6 x 10, 6 x 8, 6 x 7, 6 x 5, or 6 x 3 depending on the location in the scan array. These blocks are further broken into quadrants, as indicated in the 6 x 10 array. In each quadrant, the spots are divided into two sets, one being the half containing the highest radiances for the 11 μm window channel H8 on HIRS2. These spots are indicated as white in the figure. Radiances for all spots in a given set are averaged together for each channel. Each 125 x 125 km area is now characterized by two sets of HIRS2 radiances for each channel. *These two sets will be referred to in the future as "two fields of view."* The differences in the radiances in these fields of view will be utilized in the cloud correction algorithm to be described later, which estimates the effective clear column radiance which would have been observed in the 125 x 125 km area if it were cloud free. For each field of view, an effective satellite zenith angle is defined as the angle whose cosine is given by the average of the cosines of all the spot satellite zenith angles in the field of view.

The 125 x 125 km quadrant in which the sounding will be performed is chosen as the one containing the warmest field of view as measured by the HIRS 11 μm window channel. The latitude and longitude of the centroid of this quadrant is taken to be the location of the sounding which will be performed. The HIRS2 observations in this quadrant are also colocated with the MSU observations whose centroid is closest to that of the quadrant, and with initial esti-

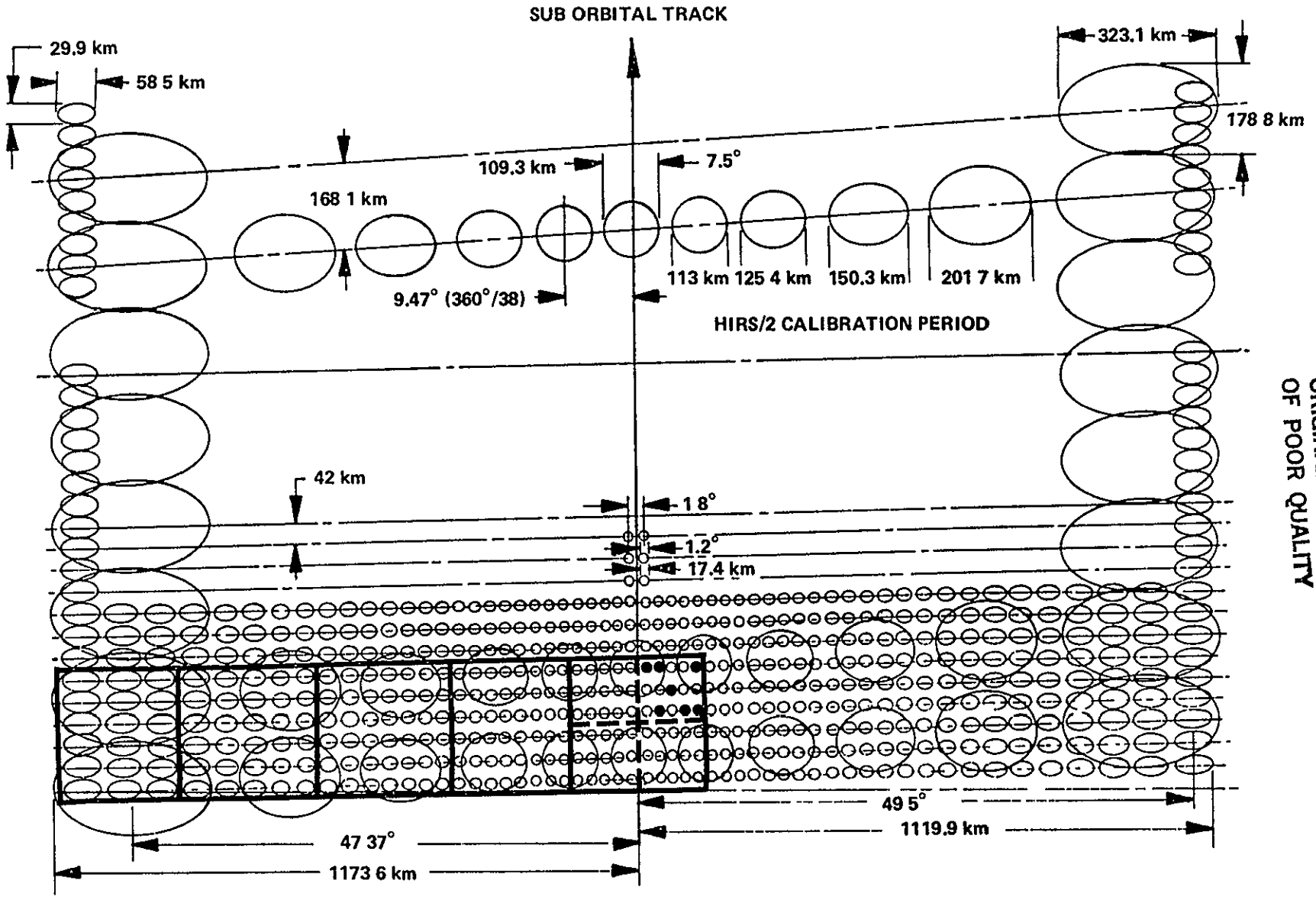

Fig. 1. Scan pattern for HIRS2 (small spots) and MSU (large spots). One retrieval is performed every 250 x 250 km (solid line box) area in one of the 125 x 125 km (dashed line box) quadrants. HIRS spots in each quadrants are averaged into 2 fields of view according to the warmest and coldest radiances from the 11μm window channel. The closest MSU spot is assigned to the quadrant.

mates of temperature profile, humidity profile, and surface pressure obtained from interpolating a 6 hour forecast generated by the GLAS GCM [Kalnay-Rivas et. al., 1977; Kalnay-Rivas and Hoitsma, 1979] to the appropriate location and time.

The preparation of data, which represents steps 1-3 described above, associates in every 250 x 250 km area observed by the satellite a time, latitude and longitude, 2 sets of HIRS2 radiances and zenith angles, a set of MSU radiances and an MSU zenith angle, and model generated estimates of surface pressure, humidity profile, and temperature profile for the selected quadrant. This is sufficient information for analysis of the data. In addition, the area contains the HIRS2 radiances in the single coldest field of view in the 250 x 250 km area, as seen by the 11μm window, and the average HIRS2 radiances for all spots in the 250 x 250 km area. These will be used in generating an effective cloud height and cloud fraction for the entire area.

3.3 Computation and Significance of the Surface Emissivity at 50.3 GHz

Steps 4 in the processing scheme, dealing with the computation of channel average radiances from atmospheric and surface conditions has been treated in detail in Chapter 1. The calculation of accurate radiances as a function of surface and atmospheric conditions is essential for all subsequent steps in the processing system.

The emissivity of the surface in the microwave region is much more variable than in the infra-red. At 50 GHz, the emissivity is typically .45 - .65 for open ocean, increasing with decreasing temperature and increasing wind speed, and .90 - .95 for land. Sea ice has an emissivity of .70 or more, depending on its history, and snow has an emissivity of .90 or less depending on the depth (Staelin, 1981).

Given a temperature-humidity profile and a surface temperature and pressure, the microwave brightness temperature at a given zenith angle is much more

sensitive to the surface emissivity than an equivalent infra-red channel would be [Kornfield and Susskind, 1977]. For accurate calculation of brightness temperatures in microwave channel 2, which has about a 10% contribution from the surface, a precise knowledge of the microwave surface emissitivity is needed. This parameter in turn also provides important information about the surface properties.

The microwave emissivity is calculated from the 50.3 GHz channel, as part of the iterative scheme, according to

$$\varepsilon = \frac{R_i - \int T d\tau - R_i^{\downarrow} \tau_i(P_S)}{[T_S - R_i^{\downarrow}] \tau_i(P_S)} \qquad (3.1)$$

where R_i is the 50.3 GHz observed brightness temperature, T_S is the iterative surface temperature, and T(P) is the iterative atmosperic temperature profile used in the calculation of the upward and downward microwave fluxes emitted by the atmosphere. The transmittance functions are corrected for temperature, water vapor, and zenith angle as described in Chapter 2, but possible effects of liquid water attenuation on the 50.3 GHz channel are not accounted for. It is assumed that in areas containing significant atmospheric liquid water, the retrieval would be rejected either on the basis of too much cloudiness or for non-convergence of the solution as explained later. The emissivity determined from the 50.3 GHz channel observation is used, together with the iterative temperature profile, and surface temperature, to calculate brightness temperatures for the other MSU channels.

3.4 Accounting for Effects of Clouds on the Infrared Observations

The radiance observed in an otherwise homogeneous field of view, containing partial homogeneous cloud cover α, is given, within a reasonable approximation by

$$R_i = \alpha R_{1,CLD} + (1 - \alpha) R_{1,CLR} \qquad (3.2)$$

where $R_{1,CLD}$ and $R_{1,CLR}$ are the radiances which would have been observed if the field of view were completely cloudy or clear, respectively. Computation of clear-column radiances $R_{i,CLR}$ can be done routinely as in equation 1.1, but computation of $R_{1,CLD}$ requires accurate knowledge of the optical as well as the meteorological properties of the cloud. It is more advantageous to be able to account for the effects of clouds indirectly than to have to model their radiative transfer properties. As shown by Smith (1968) and Chahine (1974), an estimate of the clear-column radiance, $\tilde{R}_1$, can be reconstructed from the observations in the two fields of view according to

$$\tilde{R}_1 = R_{i1} + \eta[R_{i,1} - R_{i2}] \tag{3.3}$$

where R_{1j} is the observation for channel i in the field of view j and η is given by $\alpha_1/(\alpha_2-\alpha_1)$. The fields of view are numbered in the sense that $R_{8,1} > R_{8,2}$. Once η is determined, clear-column radiances can be reconstructed from the observations by using equation 3.3. An estimate of η is obtained with each iteration.

It is seen from equation 3.3 that large values of η will tend to amplify noise in the observations and are, therefore, undesirable. In the other extreme, $\eta = 0$ implies field of view 1 is clear and $\eta = -0.5$ is taken when it appears both fields of view are clear. As shown by Chahine [1974] and Halem et al., [1978], η can be determined from the infra-red observations as part of an iterative scheme according to

$$\eta^N = \frac{R_7^N - R_{7,1}}{R_{7,1} - R_{7,2}} \tag{3.4}$$

where R_7^N is the computed clear-column radiance for the 15μm surface channel, using the Nth iterative temperature profile. In this case, the scheme will converge provided only 4.3μm infrared channels are used for temperature sounding in the lower troposphere. The rate of convergence increases with the difference

between the surface temperature and the cloud-top temperature. Under some high noise, low contrast conditions, divergent solutions can occur in the sense that an overestimate of η^N will cause an overestimate of the reconstructed 4.3μm. Clear-column radiances which, in turn, will yield an increased lower tropospheric temperature, produce an increased value of R_7^{N+1}, and lead to an increased η^{N+1}, etc.

When a lower tropospheric-sounding microwave channel is available, such as channel M2, a superior method for determing η can be used, making the estimate of η less sensitive to guess errors and alleviating the need for use of 15μm channels, which are significantly affected by H_2O and O_3 absorption, in cloud filtering. η is determined as in equation 3.4 but with the 4.3μm surface channel, 13, used instead of channel 7. The microwave channel is used to correct errors in R_{13}^N due to errors in the iterative temperature profile. The error in η^N determined from equation 3.4 is a result of either use of an incorrect temperature profile to estimate the clear column radiance, computational uncertainties such as the effect of water vapor on the transmittance functions of channel 13, observational errors in $R_{13,1}$, or errors in the assumption of only one degree of non-homogeneity in the combined fields of view. The error in R_{13}^N due to a wrong temperature profile can be well accounted for by adjusting the computed brightness temperature (equivalent black body temperature) for channel M2 according to

$$T_{13} - T_{13}^N = T_{M2} - T_{M2}^N \tag{3.5}$$

where T_{M2} and T_{M2}^N are the observed and calculated microwave brightness temperatures, T_{13}^N is the calculated clear-column brightness temperature for channel 13, and T'_{13} is the corrected clear-column brightness temperature for chan-

nel 13. This correction is based on the approximation that a bias in the iterative temperature profile in the mid to lower troposphere will produce approximately the same error in computed brightness temperature in infra-red and microwave channels sounding that portion of the atmosphere. The corrected clear-column radiance for channel 13 is then given by

$$R'^{N}_{13} = B_{13}[T^{N}_{13} + T_{M2} - T^{N}_{M2}] \tag{3.6}$$

and η is now computed according to

$$\eta^{N} = (R'^{N}_{13} - R_{13,1})/(R_{13,1} - R_{13,2}) \tag{3.7}$$

If the observations in the two fields of view are sufficiently close, most likely both fields of view are either clear or overcast. We discriminate these two cases by comparing T'_{13}, the corrected clear column brightness temperature for channel 13, to $T_{13,1}$, the observed brightness temperature for field of view 1. If $T'_{13} - T_{13,1} > 8°C$ and $\eta^{N} > 4$, the fields of view are considered too cloudy to do a retrieval. In the other limit, if $\eta^{N} < 0$ and $|T_{13,1} - T_{13,2}| < 1°C$, η is taken as -0.5, that is both fields of view are considered clear.

Utilization of the microwave observation not only speeds up convergence under all conditions, but stabilizes the solution in the sense that a positive bias in the iterative temperature profile in the lower troposphere will not, to a first approximation, cause an increase in η. The actual estimate of the cloud height and amount is performed after the final solution is obtained and will be described later. The microwave correction was not employed in chapter 1, dealing with comparison of computed and reconstructed radiances in cloudy conditions, because the true temperature profile was known.

3.5 Determination of Sea-Surface Temperatures and Ground Temperatures

The main factors influencing the accuracy of retrieved sea-surface temperatures from infra-red window observations are the effects of clouds and

humidity on the observations. Operational surface temperature sounders, such as AVHRR, utilize very fine spatial resolution observations, of the order of 1 km x 1 km, in an attempt to find completely clear spots. The current analysis, using combined infrared and microwave observations, does not require high spatial resolution nor the existence of clear spots for the determination of accurate sea or land surface temperatures, which are determined as an integral part of sounder processing system. The effects of clouds on the observations are accounted for by use of equations 4, 7 and 8, giving the clear column radiances for all infra-red channels. The two 3.7μm window channels on HIRS2, whose brightness temperatures are relatively insensitive to humidity, are used for determination of surface temperature rather than the 11μm window, which has been used operationally on AVHRR.

Given η^N, the clear radiances, $\tilde{R}_i^N$, for the two 3.7-μm window channels, 18 and 19, are reconstructed according to equation 4. At night, the reflected solar radiation term can be neglected from equation 1 and surface temperatures are easily obtained from each channel as

$$T_{s,i}{}^N = B_i{}^{-1}\left[\frac{\tilde{R}_i^N - (1-\varepsilon_i)R_i{}^{N}{}_{\downarrow}\tau_i{}^N(P_s) - \int_0^{\tau_i(Ps)} B_i(T^N)d\tau}{\varepsilon_i \tau_i{}^N(P_s)}\right] \tag{9}$$

The downward flux, $R_i{}^{N}{}_{\downarrow}$, is approximated as

$$R_i{}^{N}{}_{\downarrow} = 2\cos\theta \int_0^{\tau_i(Ps)} B_i(T^N)d\tau. \tag{3.9}$$

This approximation is based on the assumption of an optically thin atmosphere and a Lambertian surface. In general, $T_{s,18}$ and $T_{s,19}$ are found to agree

with each other to 1°C, even under partially cloudy conditions. The surface temperature, T_s^N, is taken as $1/2[T_{s,18}^N + T_{s,19}^N]$.

During the day, the effects of solar radiation on the 3.7μm channels must be accounted for in obtaining accurate surface temperature retrievals from these channels. The solar radiation reflected off clouds in the field of view has already been accounted for by the clear column radiance algorithm. If additional clouds are in the path of incident solar radiance with cloud fraction c, the solar radiation striking the ground will be attenuated by (1-c). The solar radiation reflected off the clouds will not be seen by the instrument because of its narrow field of view. The net effect is to reduce the solar radiation by a factor of (1-c).

One can attempt to account for reflected solar radiation directly by subtracting $\rho'_1 H_1 \tau_1'(P_S)$ from $\tilde{R}_1^{(N)}$ and substituting the result into equation 3.8. In the case of c=0, $H_i \tau_i'(P_S)$, the mean solar radiation across the channel traversing the path from the sun to the earth and back to the satellite, can be well estimated as $2.16\pi \times 10^{-5} B_1[5600\ K] \cos\theta_H \tau_1(P_s, \theta_{EFF})$ where θ_H is the solar zenith angle and the transmittance is computed at an effective zenith angle, θ_{EFF}, whose secant is given by the sum of the secants of the solar and the satellite zenith angles. The case of c≠0 is equivalent to an effective reflectivity $\bar{\rho} = \rho'(1-c)$.

This procedure is impractical because of the uncertainty in $\bar{\rho}_1$, even if c=0. If the surface is Lambertian and the emissivity is known, ρ'_1, the directional reflectance, is equal to $(1 - \varepsilon_i)/\pi$. Significant errors of up to a factor of 2 can be made in these estimations of ρ'_i, which may produce errors of up to 10°C in retrieved surface temperature. These errors arise from uncertainties in ε_1 and the non-Lambertian character of the surface. The same uncertainties in ε_i, however, do not appreciably affect the

calculated thermal radiation. Estimated values of 0.85 over land and 0.95 over ocean are used in the analysis. Rather than assume a value for ρ, T_s and $\bar{\rho}$ are solved for in an iterative manner, assuming only that $\bar{\rho}$ is the same for both 3.7μm channels.

For 3.7μm sounding channel 1, we can write

$$\frac{\tilde{R}_i^N - R_{ATM,1}^N}{\varepsilon_i \tau_1^N(P_s)} = B_i(T_s) + d_i H_1' = A_i^N \qquad (3.10)$$

where $R_{ATM,1}$ is the atmospheric contribution to the calculated clear-column radiance, $d_i = \bar{\rho}/\varepsilon_1$, and H_i' is given by $H_i' = H_1 \tau_i'(P_s)/\tau_i(P_s)$. The left-hand side of equation 11, and consequently A_i, is known in a given iteration. Assuming $\bar{\rho}_1$ and ε_1 are the same for both 3.7μm channels, one obtains the equation

$$B_1(T_s) - aB_j(T_s) = A_i - aA_j = A \qquad (3.11)$$

where $a = H_i'/H_j'$. This non-linear equation in one unknown, T_s, is solved iteratively according to

$$\frac{e^{-h\bar{\nu}/T_s^{M+1}}}{e^{-h\bar{\nu}/T_s^{M}}} = \frac{A}{B_1(T_s^M) - aB_j(T_s^M)} \qquad (3.12)$$

where $\nu = (\nu_i + \nu_j)/2$. This procedure converges rapidly. Once T_s is determined, d is calculated from equation (3.10). This provides a value of $\bar{\rho}$ which is used in equation 1 to correct the 4.3-μm channels for reflected solar radiation effects.

The iterative ground temperature is used to compute the estimated clear column radiances, R_i^N, for each channel. Temperature profiling utilizes a comparison of these radiances computed for the temperature sounding channels

from T_s^N and $T^N(P)$ to the Nth reconstructed clear column radiances, $\tilde{R}_1^N$. The differences are used to update the temperature profile. Over ocean, climatological sea-surface temperatures have accuracies of better than 2°C and can serve reasonably well for the computation of clear column radiances. Under conditions when it is felt that it is too cloudy to retrieve sea-surface temperatures of greater accuracy than climatology, the sea-surface temperature is fixed at its climatological value for the purpose of radiative transfer calculations. This decision is made only in the first iteration. Climatology is used if either $\tilde{T}_{18} - T_{18,1} > 20°C$, or $|T_s - T_{CLIM}| > 5°C$, or both $\tilde{T}_{18} - T_{18,1} > 10°C$ and $|T_s - T_{CLIM}| > 3°C$, that is, either the reconstructed brightness temperature is very far from the observed brightness temperature, indicating a large cloud correction is necessary, or the retrieved sea-surface temperature differs significantly from climatology, indicating a potential problem. If both indicators of a problem exist, the tolerance conditions made are more stringent. During the day, the same criteria are used with the 11μm window channel 8. The sea-surface temperature is fixed to climatology about 3% of the time.

The accurate a-priori knowleged of the sea-surface temperature is also used to indicate low level overcast which may have been missed by the cloud algorithm test for overcast described previously. If $T_s - T_{CLIM} < -3°C$ and $|\tilde{T}_{18} - T_{18,1}| < 2 | T_s - T_{CLIM}|$, that is the retrieved sea-surface temperature is more than 3° colder than climatology and the difference is greater than half the difference in reconstructed and observed brightness temperatures, the fields of view are considered to be full overcast with low level clouds. No retrieval is performed under these conditions. The retrieval is also rejected if the final retrieved sea-surface temperature differs from climatology by more than 5°.

3.6 The Atmospheric Temperature Relaxation Equation " The Inverse Problem"

Forms of the relaxation method of finding a solution to a set of radiative transfer equations was developed by Chahine (1968, 1970) and Smith (1970). It differs from other methods in that it does not attempt, in any iteration, to find a best solution to the set of equations (observations) but only to provide a set of parameters giving better agreement of observed and calculated radiances than obtained in the previous iteration. The iterative method is computationally fast and stable. Moreover, to solve the inverse radiative transfer equation it is necessary first to put the equation in approximate linear form with coefficients which are profile-dependent. Therefore, an "exact" solution must be iterative in any event.

In the iterative relaxation scheme, modifications to the temperature profile are made according to the differences of observed and computed radiances in temperature sounding channels weighted by the sensitivity of observations in these channels to changes in temperature in different parts of the atmosphere. Given $\tilde{R}_i^N$ and R_i^N, it is most convenient to compare the reconstructed and computed brightness temperatures, $\tilde{T}_i^N$ and T_i^N, because of an essentially linear relationship between changes in brightness temperature with changes in temperature profile.

The differences between $\tilde{T}_i^N$ and T_i^N are used both to compute the next iterative temperature profile and to decide when to terminate the iterations. The iterative procedure is terminated if the root mean square differences of $\tilde{T}_i^N$ and T_i^N for the temperature sounding channels is not at least 5% lower than in the previous iteration. Also, a maximum of 10 iterations is performed. When the iterative procedure is completed, the retrieval is rejected as non-convergent if this RMS difference is not less than 1°C. In addition, the

retrieval is rejected as non-convergent if the computed brightness temperature for microwave channel 2, which gives a measure of the mean tropospheric temperature, differs from the observation by more than 1°C. This channel, which is not used directly in the solution of the relaxation equations, gives a good check on the consistency of the solution with an additional observation. Microwave channel 2 is used indirectly through the cloud filtering algorithm as shown in equation (3.6). The frequency of occurence of non-convergence is roughly independent of cloud cover, but a tendency occurs for rejection when the microwave observations with the largest zenith angle are used.

In order to use the difference of reconstructed and computed brightness temperatures in the temperature sounding channels to estimate the error in the Nth iterative temperature profile, it is useful to look at the response of the brightness temperature of a channel to changes in atmospheric temperature profile.

From equation (1.1), we see that to a good approximation, brightness temperatures for two closely related temperature profiles, T(P) and T(P)+ δ (P), will differ by

$$T_1[T(P) + \delta(P)] - T_1[T(P)] = \int W_1(P)\ \delta(P)\ d\ln(P) \tag{3.13}$$

where

$$W_1(P) = \left(\frac{dT_1}{dR_1}\right)_{R_1} \left(\frac{dR_1}{dT}\right)_{T(P)} \tag{3.14}$$

$$= \left(\frac{dT}{dB_1}\right)_{T_1} \left(\frac{dB_1}{dT}\right)_{T(P)} \left(\frac{d\tau_1}{d\ln p}\right)_{P}$$

assuming all else remains constant. Figure (2) shows the weighting functions which, as defined in equation 3.14, relate the change in brightness temperature to the change in atmospheric temperature profile, for the seven channels used

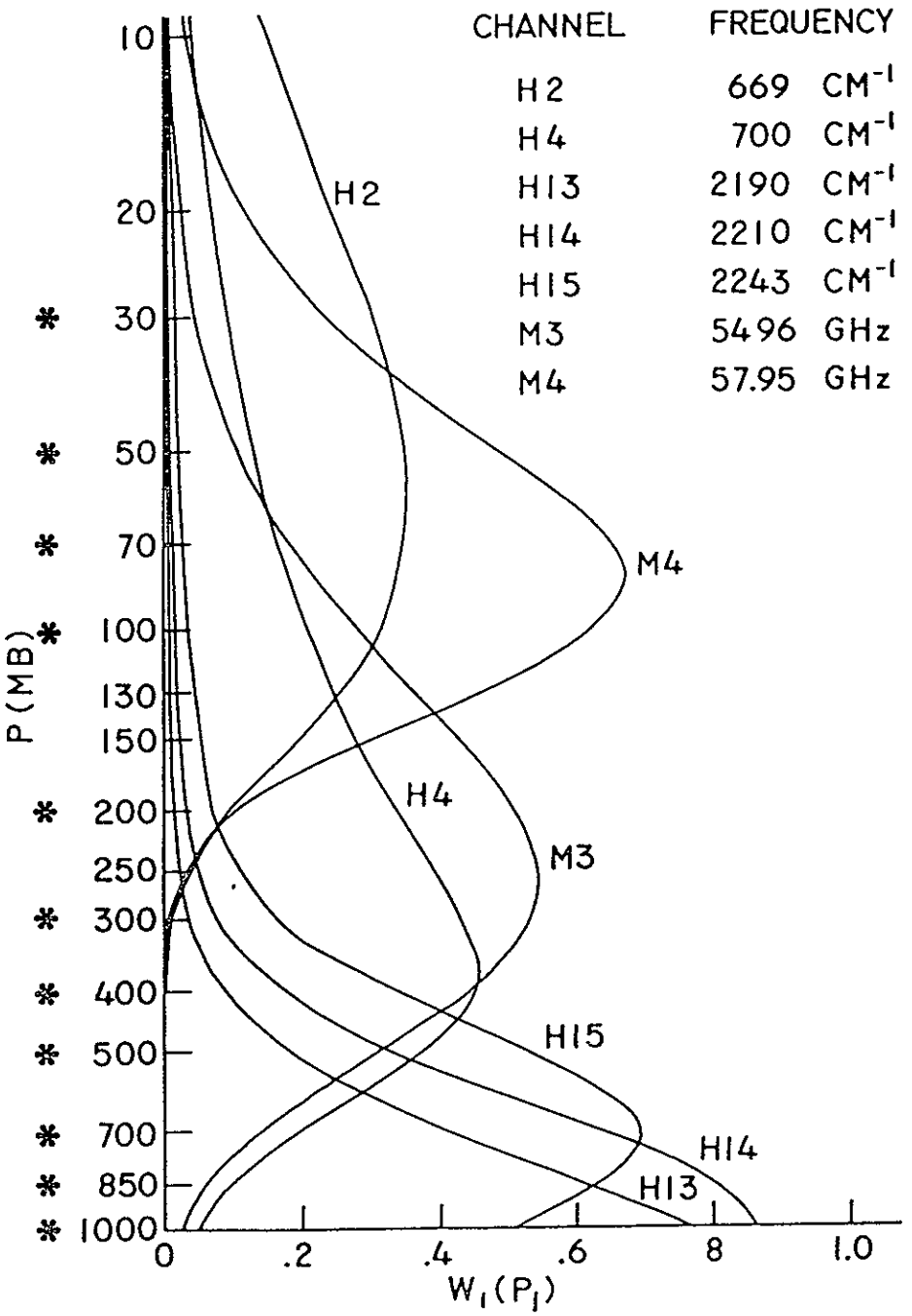

Fig. 2. Weighting functions, for a U.S. standard atmsophere at nadir viewing, for the seven HIRS2-MSU channels used to determine the temperature profile. These channels are used to estima mean temperatures for the layers bounded by *.

in determining the atmospheric temperature profile.

It can be shown that

$$\int W_1(P)d\ln(P) \approx 1 - \tau_1(P_S) \tag{3.15}$$

Therefore, to a good approximation, for two profiles differing by a constant, δ,

$$T_1[T(P) + \delta] \approx T_1[T(P)] + \delta\ (1 - \tau_1(P_S)), \tag{3.16}$$

that is, a constant shift of temperature profile throughout the atmosphere produces approximately the same change in brightness temperature, reduced by a small amount if the channel sees the surface. Moreover, if we look, for example, at channel M4 in Figure (2), we see the brightness temperature in that channel is virtually independent of temperatures above 10 mb and below 300 mb and is mostly dependent on temperature between 40 mb and 130 mb. Therefore, we can attribute a difference, δ between observed clear-column brightness temperature, T_{M4}, and computed brightness temperature, T^N_{M4}, to a comparable difference in the true layer mean temperature 130 mb and 40 mb, $\overline{T}_1 = \int \overline{T}(P)\ d\ln P$, and that of the Nth guess.

In order to reduce the effects of noise and stablizes the solution, it is desirable to average the estimates of mean layer temperature

$$\overline{T}_1^{N+1} = \overline{T}_1^{N} + \sum_J \overline{W}_{1J}\ [\tilde{T}_J^{N} - T_J^{N}] \ /\ \sum_J \overline{W}_{1J} \tag{3.17}$$

where $\overline{W}_{1J}$ is the mean value of $W_1(P)$ in layer 1. There is no need for a one to one relationship between the number of channels and number of layers.

In the analysis, mean layer temperatures for the ten layers shown in Figure (2) are used to determine the total temperature profile $T^{N+1}(P)$. To insure uniqueness, a constraint is put on the system that

$$T^{N+1} = T^G + \sum_{k=1}^{L} A_k^{N+1} F_k \tag{3.18}$$

where $T^G(P)$ is a global mean temperature profile, $F_k(P)$ are empirical orthogonal functions at 52 pressure levels extending from 1000 mb to 30 mb, given by the eigenvectors, with largest eignenvalues, of the covariance matrix of a set of global radiosonde profiles, and A_k^{N+1} are iterative coefficients. The coefficients A_K uniquely define the solution.

The L coefficients, A_k^{N+1} can be determined for each iteration from the N+1 estimate of M mean layer temperatures, T^{N+1}, and any other information we may have. If for example, we want to find the L coefficients that compute mean layer temperatures that agree to the M specified values best in a least square sense, then

$$A^{N+1} = (\overline{F}'\overline{F})^{-1}\overline{F}'\Delta^{N+1} \tag{3.19}$$

where A is the vector of L coefficients, $\overline{F}$ is an M by L matrix with elements $\overline{F}_{ik}$ given by the mean value of $F_k(P)$ in layer i, and Δ_i^{N+1} is the difference between T_i^{N+1} and $T_{G,i}$, the mean layer temperature of the global mean.

$$\Delta_i^{N+1} = \overline{T}_i^{N+1} - \overline{T}_{G,i} \tag{3.20}$$

Because of uncertainties in the mean layer temperatures, increased stability is obtained by finding the coefficients which minimize a combination of the difference between estimated and computed mean layer temperatures, on the one hand, and maximizes the likelihood of the solution on the other. The appropriate equation is given by

$$A^{N+1} = [\overline{F}'\overline{F} + \sigma_H]^{-1}\overline{F}'\Delta^{N+1} \tag{3.21}$$

where H is a diagonal M x M matrix with H_{11} being the inverse of the fraction of total variance arising from eigenvector i, and σ is a constant. In practice, equation 22 is used with six EOFs and $\sigma = 5 \times 10^{-4}$.

It is seen from Figure (2) that while very little detailed information is

contained about temperatures above 50 mb, the observations in channels 2 and M4 are still quite sensitive to temperature changes above this level. It was found that when the difference in the observed brightness for channel 2 and that computed from the first guess was more than 5°C, the retrieval was usually of poor quality at pressures less than 200 mb but satisfactory above 200 mb. These retrievals were flagged as good only in the troposphere. Occurrence is almost exclusively over land at the high latitudes.

3.7 Comparison of the Relaxation Method with Regression

The net result of equations, 3.17, 3.18, 3.20, and 3.21 is the iterative equation

$$T^{N+1} = T^N + [B-I]\ [T^N - T^G] + BW^N\ [\tilde{T}_B^N - T_B^N] \tag{3.22}$$

where T^G is the 52 level global mean temperature profile, T^N is the Nth guess temperature profile, $(\tilde{T}_B^N - T_B^N)$ is the difference between the reconstructed clear column brightness temperatures and those computed in the Nth iteration, W^N is the matrix of weighting functions, defined by equation 15 in the Nth iteration but normalized so that the sum of W over all channels equals 1 for any layer, and B is given by

$$B = F(\bar{F}'\bar{F} + {}_{\sigma}H)^{-1}\ \bar{F}'L \tag{3.23}$$

where L is the matirx which produces layer average values from point values (e.g. $\bar{T} = LT$, $\bar{F} = LF$, $\bar{W} = LW$), and 1 is identity matrix. The matrix BW is the fundamental interpolation matrix which produces a change in temperature profile given a difference between observed and computed brightness temperatures. It is composed of two elements, the profile dependant weighting functions which contain the atmospheric\physics, and the statistical B matrix which results from the constraints on the solution. The term $[B-I]\,[T^N - T^G]$ arises from the

expansion of the solution about the global mean and tends to further stablize the solution under high noise conditions. This term would drop out of equation (3.22) if T^G in equation (3.18) were replaced by T^N, i.e., if the iterative temperature profiles were constrained as an expansion about the Nth guess rather than about the global mean.

While the form of equation (3.22) is similar to that used in regression analysis, there are a number of significant differences. Foremost amoung these is that equation (3.22) contains the full physics of the problem, allows for the incorporation of initial guess information into the solution, for the iterative treatment of the effects of clouds on the radiances, and for the ability to determine whether a solution can be found with satisfactory agreement of observed and computed radiances.

3.8 Determination of Cloud Height and Amount

Given a temperature profile, an effective cloud height and percent cloud cover which match the outgoing long wave radiation can be determined by use of equations (1.1) and (3.2). The cloud height is effective because of the possibility of the presence of multiple cloud layers in the field of view. The cloud fraction is effective both for the above reason, and because it is the product of the true cloud fraction and the cloud emissivity. It represents the cloud opacity in the field of view. If we assume a single cloud layer, whose emissivity is ε_{1c} and whose top is at P_c with temperature $T(P_c)$, where $T(P)$ is the retrieved temperature profile, then equation (1) can be evaluated at any assumed cloud top pressure to give

$$R_{1,cld}(P_c) = \varepsilon_{1c}\,[B_i[T(P_c)]\tau_i(P_c) + \int_{\tau_i(P_c)}^{1} B_1(\tau)d\tau] \qquad (3.24)$$

Using equation (3.2), an effective cloud fraction consistent with the assumed cloud pressure, $\alpha_1(P_c)$, can be determined for channel i according to

$$\alpha_1(P_c) = \frac{R_{1,clr} - R_1}{R_{1,clr} - R_{1,cld}(P_c)} \tag{3.25}$$

where R_1 is the observation for channel 1 and $R_{1,clr}$ is the calculated clear column radiance using the retrieved temperature profile. For any set of channels, P_c and α can be determined which minimizes the difference between the observed and computed radiances for the channels. In the current analysis, two channels were used and α and P_c were found such that $\alpha_1(P_c) = \alpha_j(P_c) = \alpha$.

In the global retrieval program, one temperature retrieval is performed every 250 x 250 km, and is localized in the 125 x 125 km quadrant having the field of view containing the warmest observed brightness temperature. This quadrant is chosen because it is assumed to be the single least cloud contaminated field of view. If cloud parameters are retrieved from the same quadrant that the temperature field is retrieved from, the general cloudiness would be systematically underestimated. To provide an estimate of cloudiness over the entire 250 x 250 km area, radiances from all four quadrants are averaged to be used in equation (3.25) for determination of cloud fraction, given a cloud height. The retrieved temperature profile from the clearest quadrant is assumed valid for the entire 250 x 250 km area and is used in equation (3.24) to estimate the cloud radiance as a function of cloud top pressure.

To maximize stability and minimize the effects of errors and uncertainties, the numerator and demoninator of equation (3.25) should be maximized. Therefore, both the full overcast and the observed radiances should be as different as possible from the clear column radiance. For this reason, channels 6 and 7, the two 15μm channels sounding closest to the surface, are utilized for cloud height determination, and the observations used to determine cloud height are taken from the single coldest of the eight fields of view in the 250 x 250 km area. The cloud height is allowed to be between 850 mb and the tropopause.

Using this cloud height, the effective cloud fraction for the entire area is determined from the radiances of channels 6 and 7 averaged over the entire field of view.

The cloud parameters obtained are effective in the sense that they reproduce the outgoing longwave radiation but not necessarily the detailed cloudiness. Under multiple cloud layers, for example, a single intermediate cloud height would be found and the total cloud fraction would be underestimated.

If the retrieval performed in the quadrant with the warmest observation has been rejected, cloud parameters can still be determined in an identical fashion, but the initial guess is used in equation (3.25) to compute clear and cloudy radiances rather than the solution. In the special case when overcast low level cloudiness has been found, 100% cloud cover is set at the pressure at which the guess temperature is equal to the retrieved surface temperature. If this pressure is greater than 600 mb, a second layer of clouds is looked for if the brightness temperatures in the coldest field of view are significantly lower than in the warmest field of view. The procedure is identical to that described previously, but it is assumed that there is complete overcast of the lower cloud deck throughout the entire 250 x 250 km field of view and the surface contribution to equation (1.1) is taken to come from the lower cloud level rather than the earth.

This procedure can provide cloud parameters under almost all conditions. However, approximately 20% of the time, it is apparent from the observations that partial cloudiness exists, and no consistent cloud height and cloud fraction can be determined from using channels 6 and 7 and equations (3.24) and (3.25). In such situations, a cloud field is not returned. We are currently investigating a procedure to determine the amount and height of clouds by minimizing the residual of computed radiances for more than two tropospheric

sounding channels [Chahine, 1982] to produce improved cloud parameters under all conditions.

Chapter 4

Results for January 1979

4.1 Yield of Successful Retrievals vs. Cloudiness

440,000 retrievals were run for the period Jan 5 - Feb 2, 1971, with one retrieval in every grid area as shown in Figure (1). Of these, 60% were acceptable retrievals and 40% were rejected. The retrievals are broken down into quality flag vs. retrieved per-cent cloudiness in Table 4.1. The column marked % indicates the fraction of all retrievals having the appropriate quality flag. Retrievals of each quality flag are further broken down into the precentage of time they occur with a given cloud fraction. The column marked * represents retrievals in which no cloud height and cloud fraction could be retrieved. This occured about 20.6% of the time, most likely in areas containing more than one degree of homogeneity, either in the sense of multiple cloud formations or varying scenes in the clear part of the field of view. Retrievals of the first three types are all considered acceptable retrievals and statistics are also given for the total class of acceptable retrievals. Retrievals of the next four types were all rejected for the indicated reasons. Cumulative statistics are also given for all rejected retrievals as well as for all retrievals. The last row of the table, unlike the other rows, does not give the percentage of a given class of retrievals containing a given cloud amount, but indicates the percentage of all retrievals with a given cloud amount which were considered good retrievals.

A total of 60% of all retrievals were acceptable, 45% without qualification, 3% with no sea surface temperature retrieved, and 12% with no stratospheric retrieval. For the class of acceptable retrievals, 36.7% were found to be in clear cases, 21.7% were in cases where no cloud field could be produced, 25.6% were in cases with cloud fractions greater than zero but less than or equal to 40%, 15% were in cases of cloud fraction greater than 40% but less than or equal to

Table 4.1

Per-Cent Retrieval Type vs. Per-Cent Cloudiness

Quality Flag	%	FRACTIONAL CLOUD COVER											
		*	CLR	.01-.1	.11-.2	.21-.3	.31-.4	.41-.5	.51-.6	.61-.7	.71-.8	.81-.9	.91-1.0
**good retrieval	45	19.7	40.8	2.8	6.9	8.3	7.7	6.3	4.4	2.4	.7	.1	0
**good retrieval, no SST retrieved	3	23.0	18.8	2.0	4.9	6.3	8.6	10.9	12.1	9.6	3.4	.3	0
**good tropospheric retrieval	12	29.3	25.6	1.1	5.3	9.3	10.6	9.2	5.9	2.8	.8	.1	0
***too cloudy to do a retrieval	4	2.6	.1	0	0	.1	.7	2.3	6.7	15.1	29.7	34.7	8.0
***non-convergent retrieval	28	23.6	40.1	2.0	5.0	6.5	6.5	5.7	4.6	3.7	2.0	.3	0
***low level overcast	5	0	0	0	0	0	0	0	0	0	0	0	100
***reject retrieval because of bad SST	3	26.2	16.0	1.4	6.3	10.9	12.6	12.4	9.4	4.0	.7	.1	0
all acceptable retrievals	60	21.7	36.7	2.4	6.5	8.4	8.3	7.1	5.1	2.8	.9	.1	0
all rejected retrievals	40	18.7	29.7	1.5	4.0	5.4	5.6	5.2	4.6	4.4	4.4	3.6	12.9
all retrievals	100	20.6	33.9	2.1	5.5	7.2	7.3	6.3	4.9	3.4	2.3	1.5	5.1
per cent good for given cloud fraction		63.6	65.2	71.1	71.0	70.1	69.2	67.5	62.5	49.4	23.0	.03	0

*no cloud field retrieved
**acceptable retrieval
***rejected retrieval

70%, and only 1% were in cases of cloud fraction greater than 70%. For the class of rejected retrievals, 29.7% were clear, 18.7% had no cloud field returned, 16.5% were in cases of less than 46% cloudiness, 14.2% were in cases between 40% and 70% cloudiness, and 20.9% were in case of cloudiness more than 70%. Successful retrievals outnumber rejected retrievals for all cloud fractions up to 60%, and are of comparable amount in the 60-70% range. It is interesting to note also that for up to 70% cloud cover, the majority of rejected retrievals occur because of non-convergence, and that the distribution of retrieved cloud amounts in non-convergent retrievals is similar to that in accepted retrievals. This indicates that successful HIRS2 retrievals can be performed in areas with cloud fraction of up to 70%. Retrievals indicating cloud fraction of over 70% in the 250 x 250 km area represent only 9% of the total cases.

Figure (3) indicates the distribution of successful retrievals in terms of coverage per-day on the 4° lat. x 5° lon. grid used in the GLAS general circulation model [Kalnay-Rivas et al., 1977]. Each grid point is counted 1 or 0 depending on whether a successful retrieval is found in a given 6 hour period. The maximum possible yield is, in general, 2 retrievals per day because most grid points (except for high latitude points) are covered only twice daily. As shown in Fig. 3, retrieval coverage of at least 1 time per day is almost global with the exception of a few areas where persistant cloudiness occured for moderate periods of time. Conspicuous by their absence are features due to the ITCZ or mountain areas, indicating that these factors do not significantly decrease the retrieval yield.

4.2 Temperature Retrieval Accuracy

Accuracies of the retrieved temperature profiles for Jan 5 - Feb 2, 1979 are shown in Figure (4), comparing mean layer temperatures of GLAS retrievals, in the 9 pressure intervals shown, with mean layer temperatures reported by

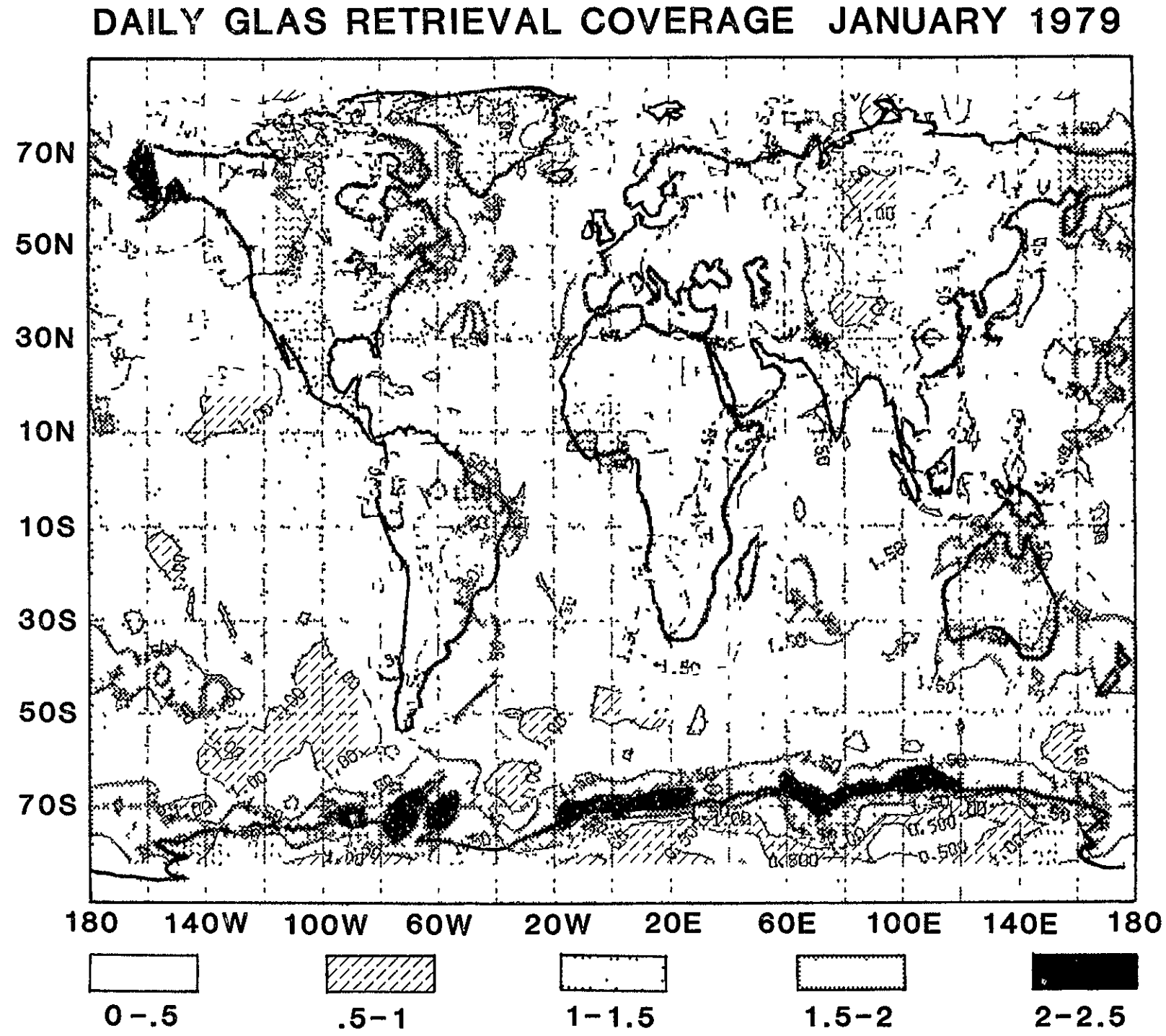

Fig. 3. Average number of times per day at least one successful retrieval was performed per six hour period in a 4° x 5° box. "Perfect" coverage is nominally 2 times per day.

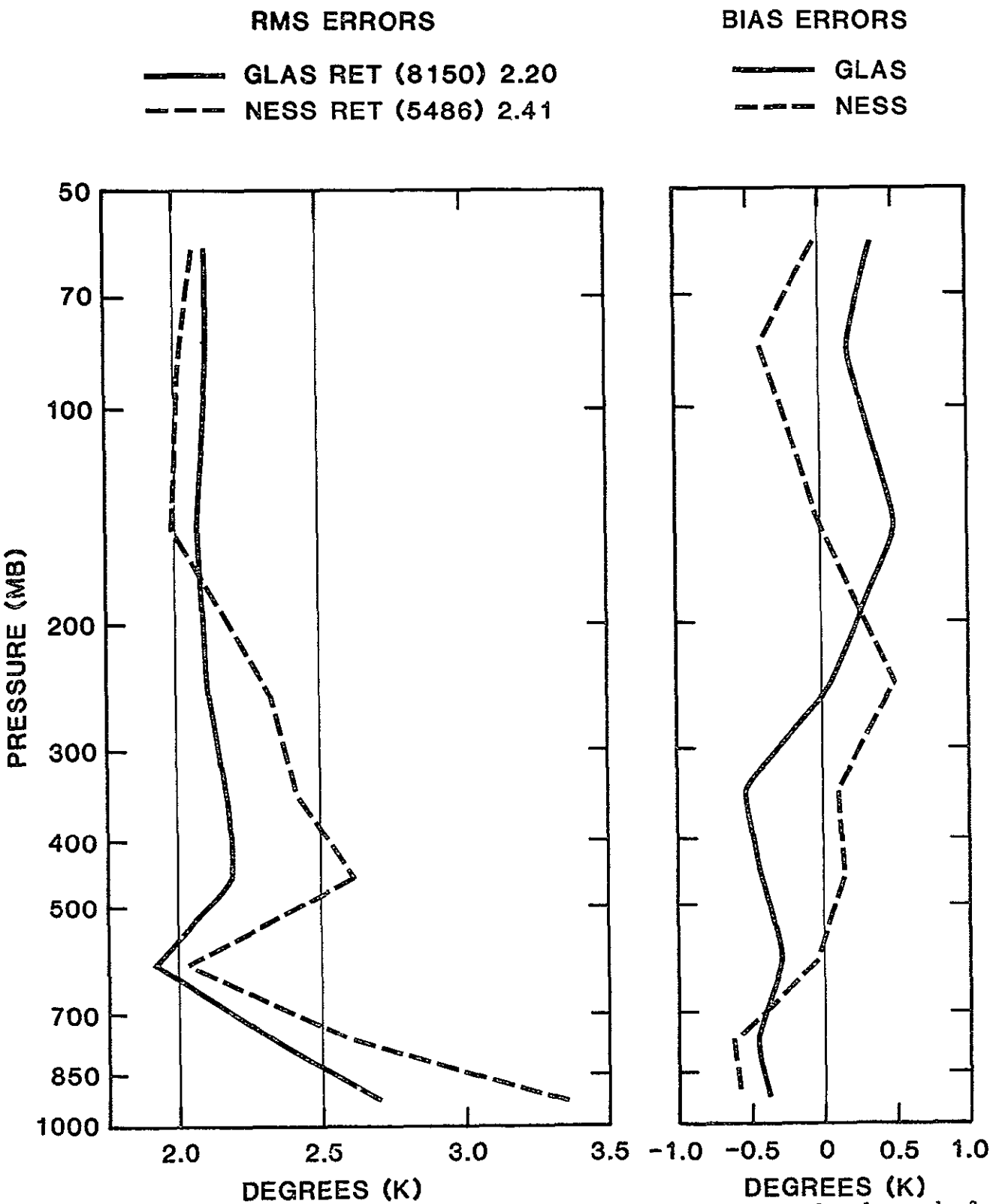

Fig. 4. Errors of retrieved mean layer temperatures compared to colocated radiosonde for January 5-February 2, 1979.

radiosondes colocated in space to 110 km and in time to 3 hr. Retrievals flagged bad are not included in the statisitics. In addition, retrievals flagged bad in the stratosphere are not included at 200 mb and above. Also shown are retrieval accuraacies of the operational NESS retrievals fdor the same period of time (subsequent to this period of time, NESS introduced changes to their operational clear column radiance algorithm [McMillin and Dean, 1982], but this new processing system has not been applied to the Jan. 1979 data). In the case of NESS retrievals, reported mean layer virtual temperatures are compared to virtual temperatures derived from the radiosonde temperature-humidity profiles. The GLAS retrievals are seen to be significantly more accurate in the troposphere, though slightly less accurate in the stratosphere. The total RMS error of the 8150 colocated GLAS retrievals is 2.20°, .21° lower than that of the 5486 colocated NESS retrievals. Also shown in Figure (4) are the bias errors of the retrievals. The GLAS retrievals tend to have a .4° cold bias in the troposphere and a .4° warm bias in the stratosphere. The causes of these biases are being investigated. A tendency has been found for the bias to disappear in clear areas and be largest in tropical cloudy areas.

Figure (5) shows a breakdown of the error statistics into categories of varying cloud cover for the period Jan 5 - 15, 1979. The NESS retrievals were stratified according to the reported retrieval type. In the retrievals marked clear NESS treated the HIRS2 observations as not cloud contaminated and they applied no cloud correction to the HIRS2 radiances. In the retrievals marked N*, NESS performed a correction to account for cloud effects on the HIRS2 observations before the retrieval was performed. In the retrievals marked cloudy, the effects of clouds on the HIRS2 observations were considered by NESS to be too large to be accurately accounted for and only HIRS2 channels 1-3, sounding the stratosphere, were used in the retrieval together with the MSU and SSU

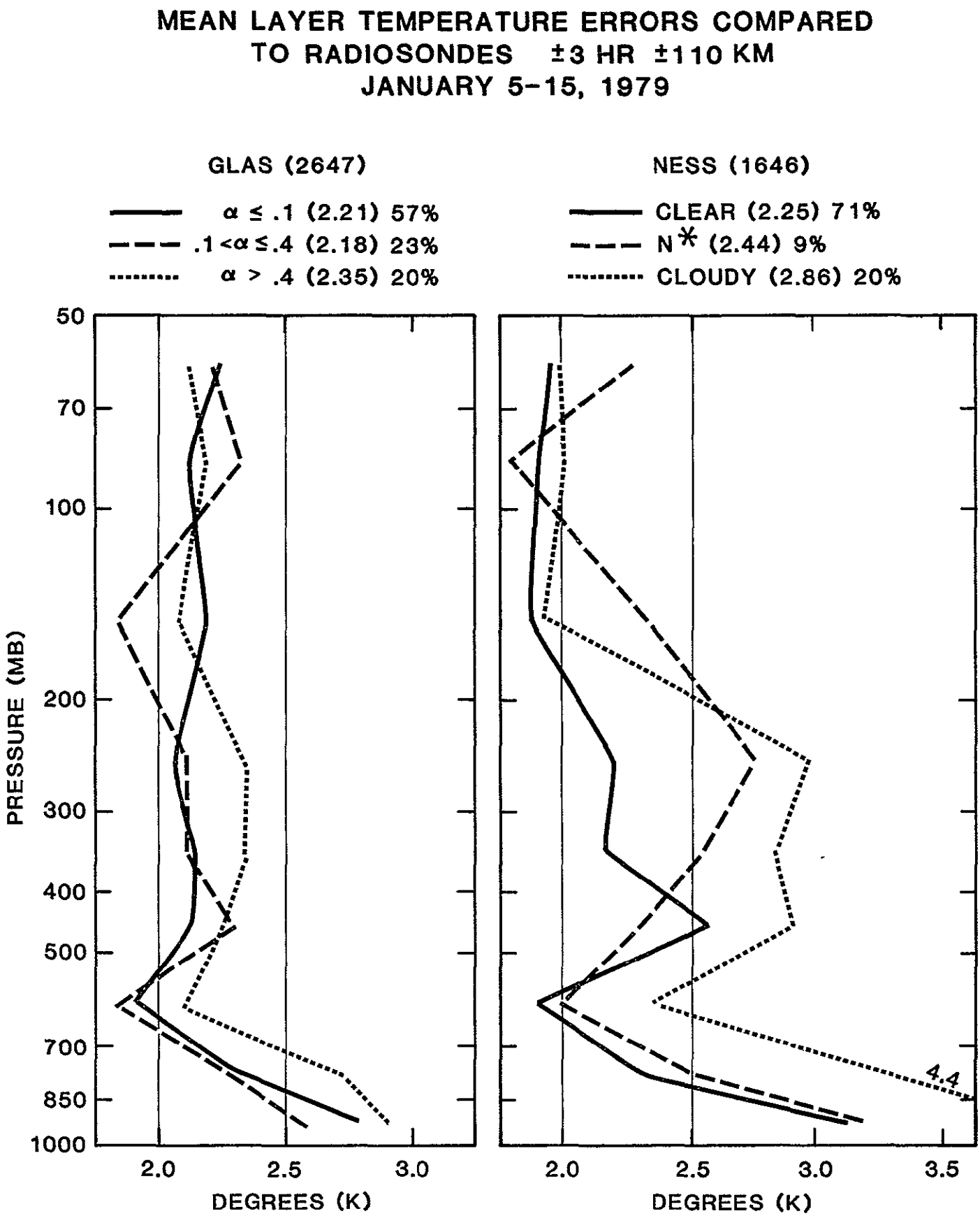

Fig. 5. Breakdown of RMS mean layer temperature errors vs. degree of cloudiness for January 5-January 15, 1979. GLAS retrievals are separated according to retrieved cloud fraction, α. NESS retrievals are separated according to reported retrieval type.

observations. The GLAS retrievals were partitioned according to almost clear ($\alpha \leq .1$), partially cloudy ($.1 \leq \alpha \leq .4$), and highly cloudy ($\alpha > .4$) conditions. The latter cutoff appears to be about the region where NESS began to apply their cloudy algorithm. NESS has a considerably higher percentage of "clear" retrievals than GLAS has. The main reason for this difference is that the GLAS cloud fraction refers to the entire 250 x 250 km area while NESS clear refers to the existence of clear 30 km spots.

The accuracy of the GLAS retrievals is seen to degrade much less with increasing cloudiness than that of the NESS retrievals. GLAS retrievals with cloud fractions between .1 and .4 are in fact quite comparable in accuracy to those obtained under clearer conditions. The NESS N* retrievals shows a large degradation over the clear retrievals in the upper troposphere, possible due to the effects of multiple cloud layers on the radiances. Such cases would hopefully be identified and flagged in the GLAS retrieval system. The NESS clear retrievals appear to degrade somewhat in the 400-500 mb layer, possibly also due to a residual cloud effect. The NESS cloudy retrievals, using only 2 microwave channels to sound the troposphere, are of significantly lower quality, primarily due to lack of data. The GLAS retrieval system shows that reasonably accurate retrievals, using both the HIRS and MSU channels, can be performed under almost all cloud conditions.

Figure (6) shows the RMS errors in the thickness between the mandatory levels and 1000 mb obtained by comparing thicknesses computed from the retrievals and those reported by the colocated radiosondes for the same period as in Figure (5). The ratio of a thickness error to the thickness is roughly proportional to the error in the average retrieved temperature in the layer to the average temperature in the layer. If the average retrieved temperature error were constant, we would expect the thickness errors to grow linearly with the log of the pressure.

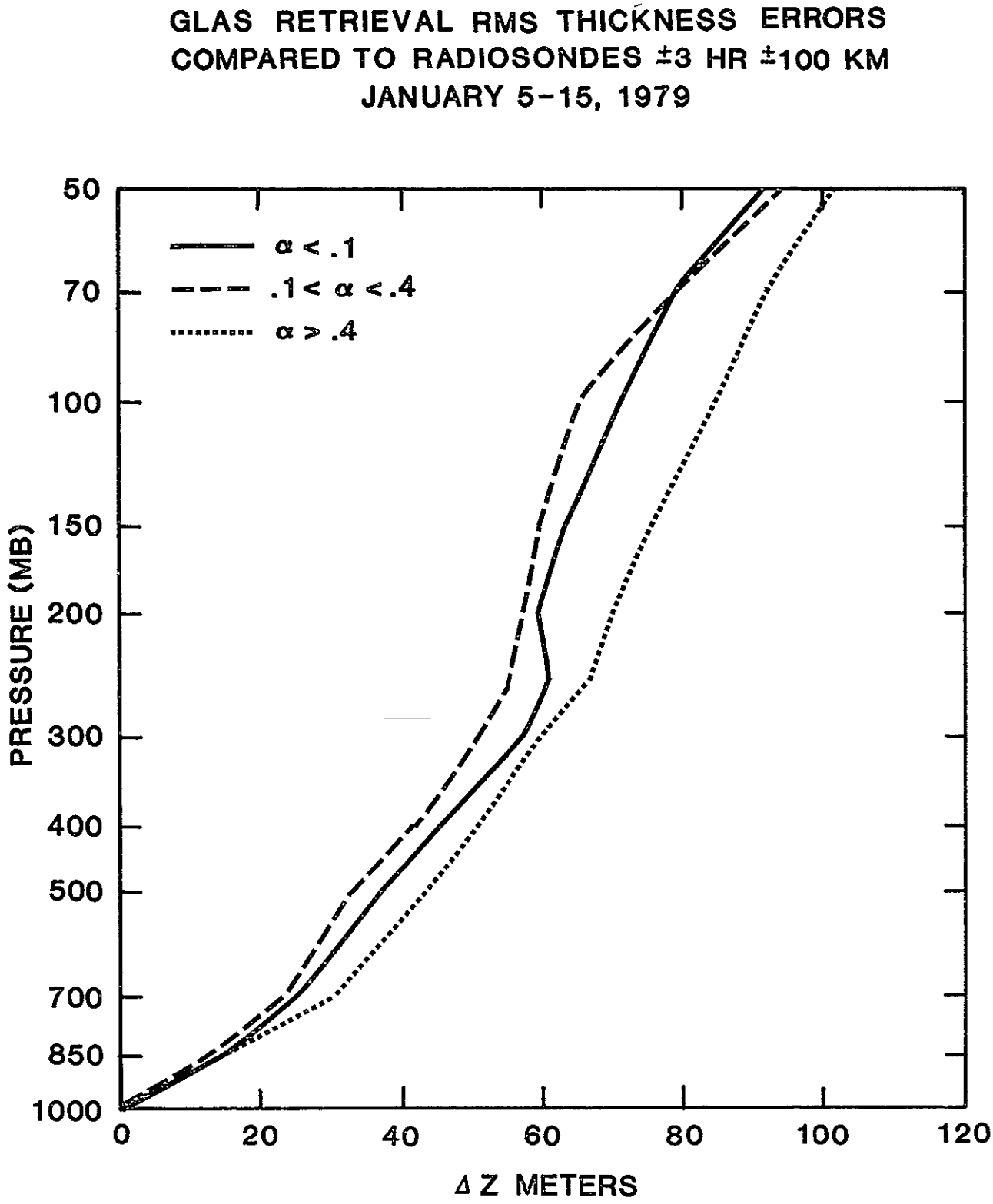

Fig. 6. RMS error of retrieved thickness between pressure P and 1000 mb compared to colocated radiosonde thickness reports, broken up according to retrieved cloud fraction, α. January 5–January 15, 1979.

The thickness errors in the GLAS retrievals appear to grow less than linearly in the log of the pressure. This implies the error in the average temperature between the surface and height z is decreasing with height, which is reasonable because of possible cancellation of errors in the detailed temperature profile. The RMS errors do not degrade appreciably with increasing cloud fraction, ranging from 33-43 meters at 500 mb, 51-59 meters at 300 mb and 65-84 meters at 100 mb. In terms of average thickness temperature errors, these values correspond to 1.6-2.1°C at 500 mb, 1.3-1.6°C at 300 mb and 1.0-1.2°C at 100 mb. The average errors decrease with height and are all considerably less than the mean layer errors shown in Figure (5).

4.3 Sea Surface Temperature Field for January 1979

The sea/land surface temperatures produced by the GLAS retrievals can be used to produce global monthly mean fields of temperatures and their diurnal variations. In particular, monthly mean sea-surface temperature fields are very significant for climatological studies. Conventional in-situ sea-surface temperature measurements from ships and buoys are numerous in the northern hemisphere but coverage is sparce in space and time in the tropics and southern hemisphere. Sea or land surface temperatures, averaged over the 125 x 125 km area, are retrieved from each successful HIRS2/MSU retrieval except those in which the sea surface temperature was held fixed at climatology. At night, equation 3.8 is used to obtain the surface temperature while equations 10-12 are used during the day. Figure (7) shows the mean sea-surface temperature field derived for the period January 5 - February 3, 1979, obtained by averaging all sea-surface temperature retrievals in 4° by 5° latitude-longitude bins. No smoothing, rejection criteria other than those described in the text, or adjustments for bias removal, were applied to the data. Differences between SST analyses using only night (3AM local time) retrievals and using

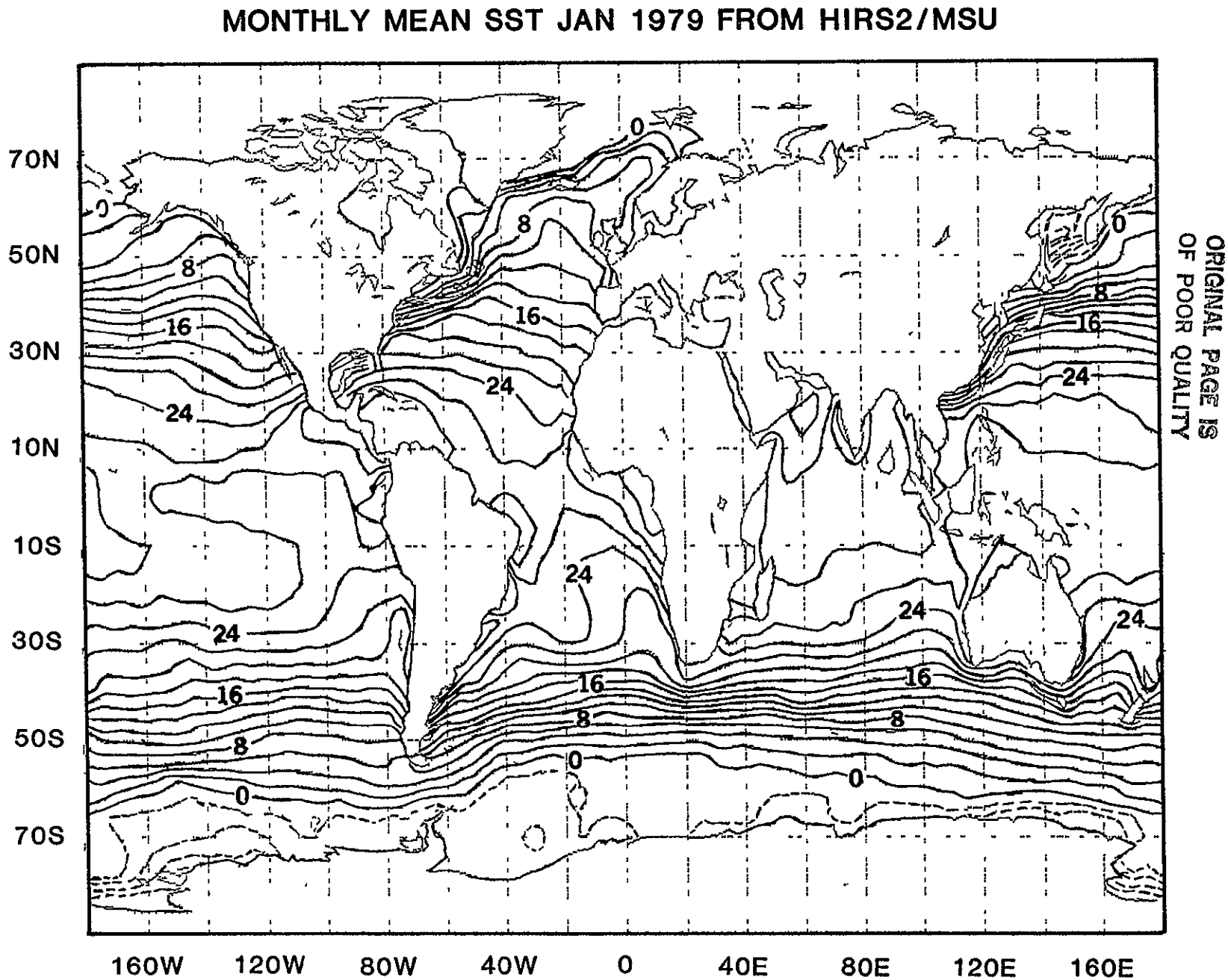

Fig. 7. Monthly mean sea-surface temperature field for January 1979, obtained by averaging all successful sea surface temperature retrievals in the 4° Lat x 5° Lon grid boxes and contouring the results. No empirical correction or filtering was done to the data. The surface temperature is determined primarily by the 3.7μm and 4.0μm window channels.

only day (3PM local time) retrievals were very small and never more than 2° in the open ocean. This indicates that the procedures used to account for the effects of solar radiation on the 3.7 μm and 4.0 μm channel observations can produce accurate daytime sea-surface temperatures using these short wave window channels. Both day and night retrievals are included in Figure (7). The major climatological sea-surface temperature features, such as the Gulf Stream, the Kuroshio, Humboldt, and Benguela currents, and the sea surface temperature minimum at the equator in the eastern Pacific are readily observable.

Of particular interest is the sea-surface temperature anomaly field for January 1979 shown in Figure (8a) obtained by subtracting the NCAR climatology, based on an average of data from 20 Januaries, from the GIAS January 1979 sea-surface temperature field. The deviations from climatology are small, being less than 2° in all cases with the exception of the centers of the warm anomaly west of South America, and the cold anomaly midway between South America and Australia.

Figure (8b) shows the anomoly field for January 1979 computed by subtracting an analysis based on ship and buoy measurements, compiled by Fleet Numerical Weather Center, from the same NCAR January climatology. The Fleet Numerical Analysis can be taken as a measure of ground truth in the areas of dense coverage. Agreement of the major anomaly features in the Northern Hemisphere, such as the cold Pacific areas, north of 40°, off the west coast of North America, and centered at 180°W, 10°N, as well as the warm Atlantic off the west coast of Africa, is excellent. In looking at this map, it should be remembered that no bias errors were removed from the retrieved sea-surface temperatures. Even small biases of a few tenths of a degree would have a significant effect on the location of the contour lines, especially the 0° bias line, which also matches extremely well. We can conclude that the absolute accuracy of the

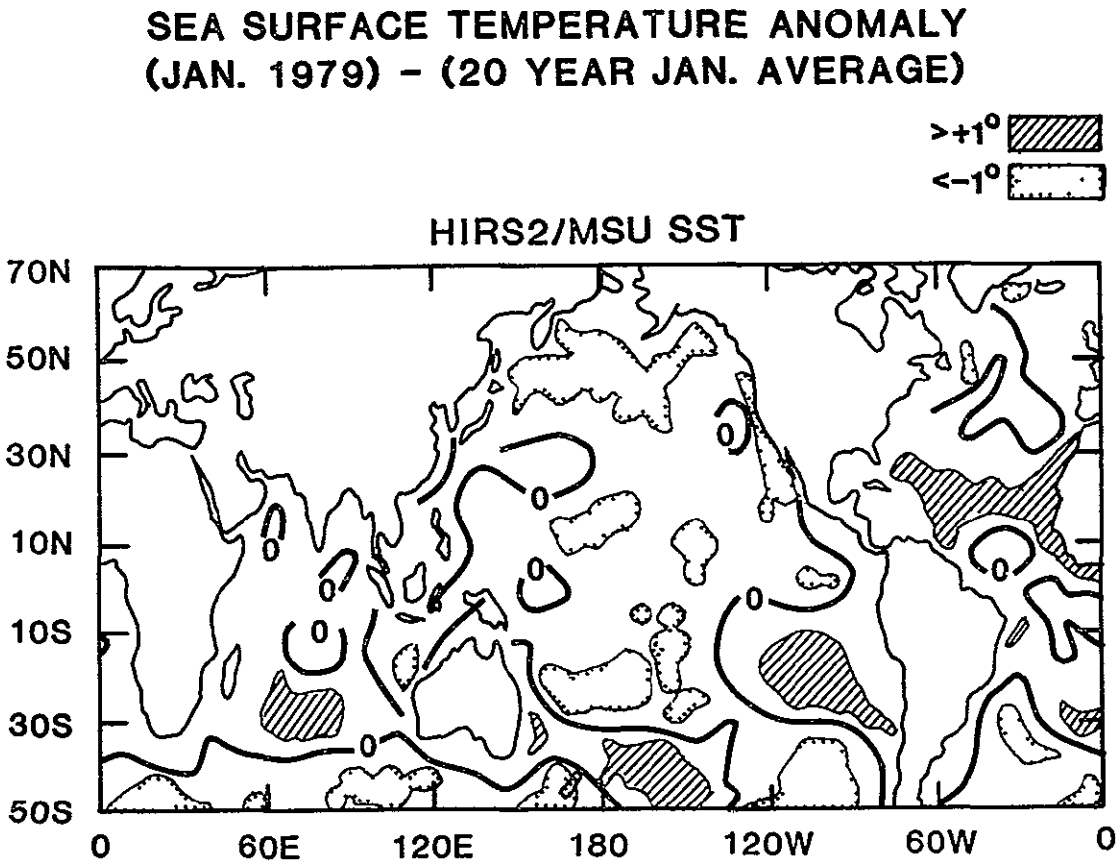

Fig. 8a. Difference between the sea surface temperature field in Fig. 7 and a climatology based on an average of 20 Januaries compiled by NCAR

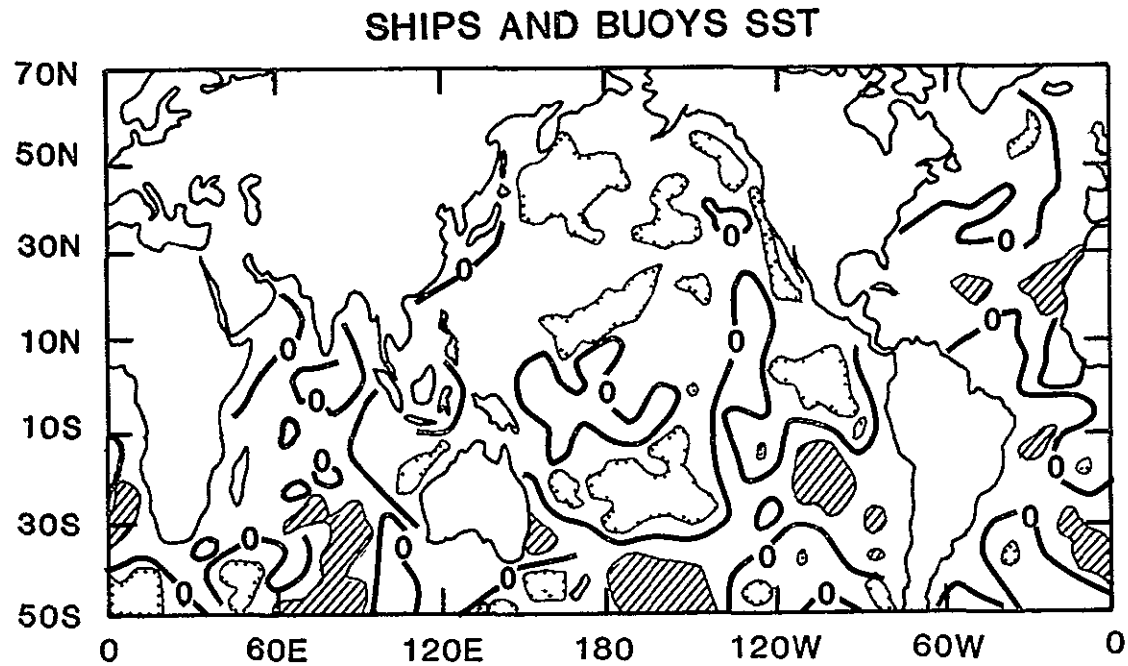

Fig. 8b. Difference between the sea-surface temperature field for January 1979, compiled by Fleet Numerical Weather Central from ship and buoy measurements, and the same NCAR January climatology.

climatolgical sea-surface temperature data is quite high. Detailed comparison of the analyses gave RMS differences of .4°C in the North Atlantic Ocean and .6° in the North Pacific.

No significant difference is found in the two fields in the tropics. This contrasts to the findings of Barnett et al., [1979], with regard to operational sea-surface temperatures in the central tropical Pacific Ocean, which are shown to have very large biases (1°-4°) compared to XBT measurements, with errors that are highly correlated with cloudiness and humidity. They concluded that the spatial structure of the error field, and the large magnitude of the errors, preclude the use of operational sea-surface temperature for climatological studies of the area. McClain (1981) has shown that improved sea-surface temperatures can be retrieved from the more recent 5 channel version of the AVHRR flying on NOAA 7 and the operational procedures have now been modified.

Agreement in the Southern Hemisphere is also extremely good. Note for example the excellent agreement of the oscillating warm, cold, warm anomaly pattern in the latitude band from 10°S to 30°S. The largest difference in the fields occurs south of 40°S, where the conventional data field is noisy as a result of sparce data. The apparent large difference in the fields between 60°E-120°E and 40°S-50°S is in fact only a 1° difference in temperatures in this area. In general the Southern Hemisphere anomaly field retreived from the satellite data is less noisy and better defined than that from conventional data.

The eastern tropical Pacific, between 10°N and 10°S, has basically no anomaly in either field. An extended warm anomaly in this area is indicative of the "El Nino" phenomenon, which has been associated with major effects on the Climate of the Northern Hemisphere [Rasmusson and Carpenter, 1982; Horel and Wallace, 1981].

Detailed analysis of specific sea and land surface temperature fields and comparisons with colocated surface measurements will be treated in a separate publication.

4.4 Effective Cloud Cover and Cloud Height for January 1979

Effective cloud heights and cloud fractions, consistent with upwelling longwave radiation, are derived for each 250 x 250 km area through use of equations (3.24) and (3.25). In the special case of low level overcast, 100% cloudiness is assigned to the level whose temperature equals the retrieved surface temperature. The cloud top pressure and cloud fraction are effective for two reasons. First, possible multiple level cloud formations are assigned a single effective cloud top pressure, which should lie somewhere in the range of the cloud top pressures in the field of view, generally close to that of the highest (coldest) clouds. Second, the effective cloud fraction is a function of the computed effective cloud top pressure for a given situation, with decreasing cloud top pressure (increasing cloud top height) corresponding to descreasing cloud fraction. Consequently, cloud cover from low level clouds may be significantly underestimated. Moreover, even for single layer clouds, the effective cloud fraction corresponds to the cloud emissivity times the actual cloud fraction. This means that cirrus clouds will be underestimated by up to a factor of 7 and mid level clouds by up to 30% [Paltridge and Platt, 1976; Chahine, 1982].

Monthly mean fields of cloud fractions, cloud top pressures, and cloud top temperatures were produced by averaging the retrieved cloud parameters in the 4° x 5° grid for the period of Janaury 5-February 2, 1979. The 20% of the cases where no cloud field was retrieved was not included in the averages. The average cloud top pressures and temperatures were taken as the average of appropriate quantities weighted by the corresponding cloud fractions. Cases

in which no cloud field can be retrieved tend to have low-intermediate total cloud cover and their omission most likely doe not significantly effect the average cloud statistics.

Figures (9a-c) show contours of average cloud top fractions, cloud top pressure, and cloud top temperature for the period. The major features such as the Intertropical Convergence Zone, the storm tracks over the Atlantic and Pacific Oceans, the oceanic deserts, and the region of the Siberian high, are clearly visible in the cloud fraction map. In the cloud top pressure map, in which only areas of high (<300 mb) and low (>600 mb) clouds have been indicated, the Intertropical Convergence Zone is again clearly visible as well as the extensive areas of predominantly stratus cloud cover below 50°S and off the west coast of the southern hemisphere continents south of 20°S. The global average effective cloud cover obtained for January 1979, sampled at 3 A.M. and 3 P.M. local time, is 25%, a value considerably lower than the accepted value of 50% global cloud cover based on ground observations [Paltridge and Platt, 1976].

The cloud top temperature field appears similar to the cloud pressure map in the tropics but very cold mid-level clouds are found in the northern hemisphere over land. It is interesting to note that the -40°C contours, corresponding to the formation of ice clouds, closely follows the continental contours in the northern hemisphere.

Verification of retrieved cloud parameters is difficult. Another representation of cloudiness for the same period is shown in Figure (10), [Gruber and Varnadore, 1981], containing the averaged outgoing longwave radiation, as determined from the 11μm channel on AVHRR on TIROS-N, for the period January 7 - January 31, 1979. In the tropics, outgoing longwave radiation is a direct qualitative measure of cloudiness because, as shown in Figure (9), areas of extensive cloudiness contain cold clouds, while clearer areas contain warm clouds or allow

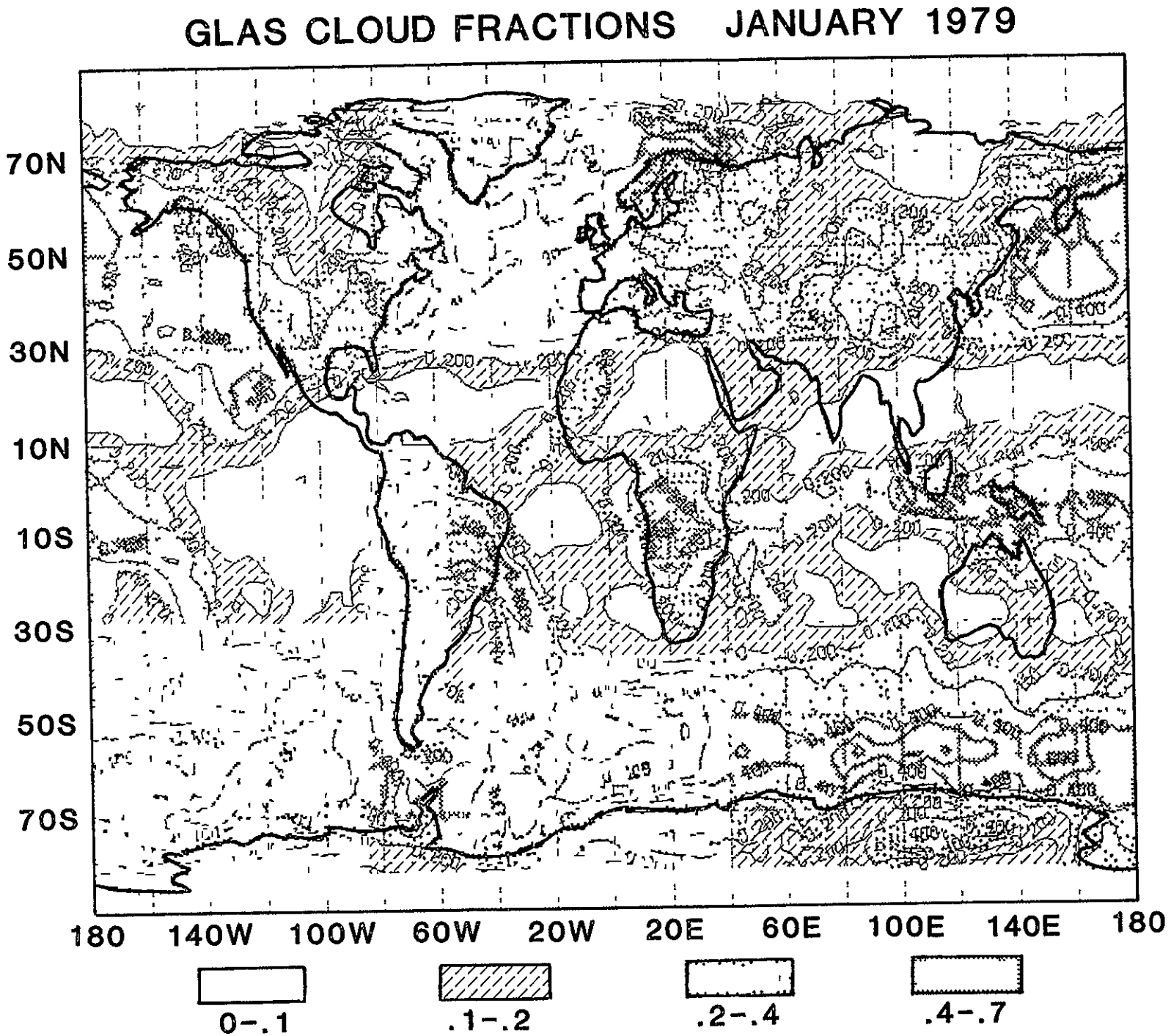

Fig. 9a. Average effective cloud fraction retrieved by GLAS for January 1979 using combined 3 A.M. and 3 P.M. soundings. The cloud parameters are determined primarily from channels 6 and 7, the two 15μm channels sounding lowest in the atmosphere.

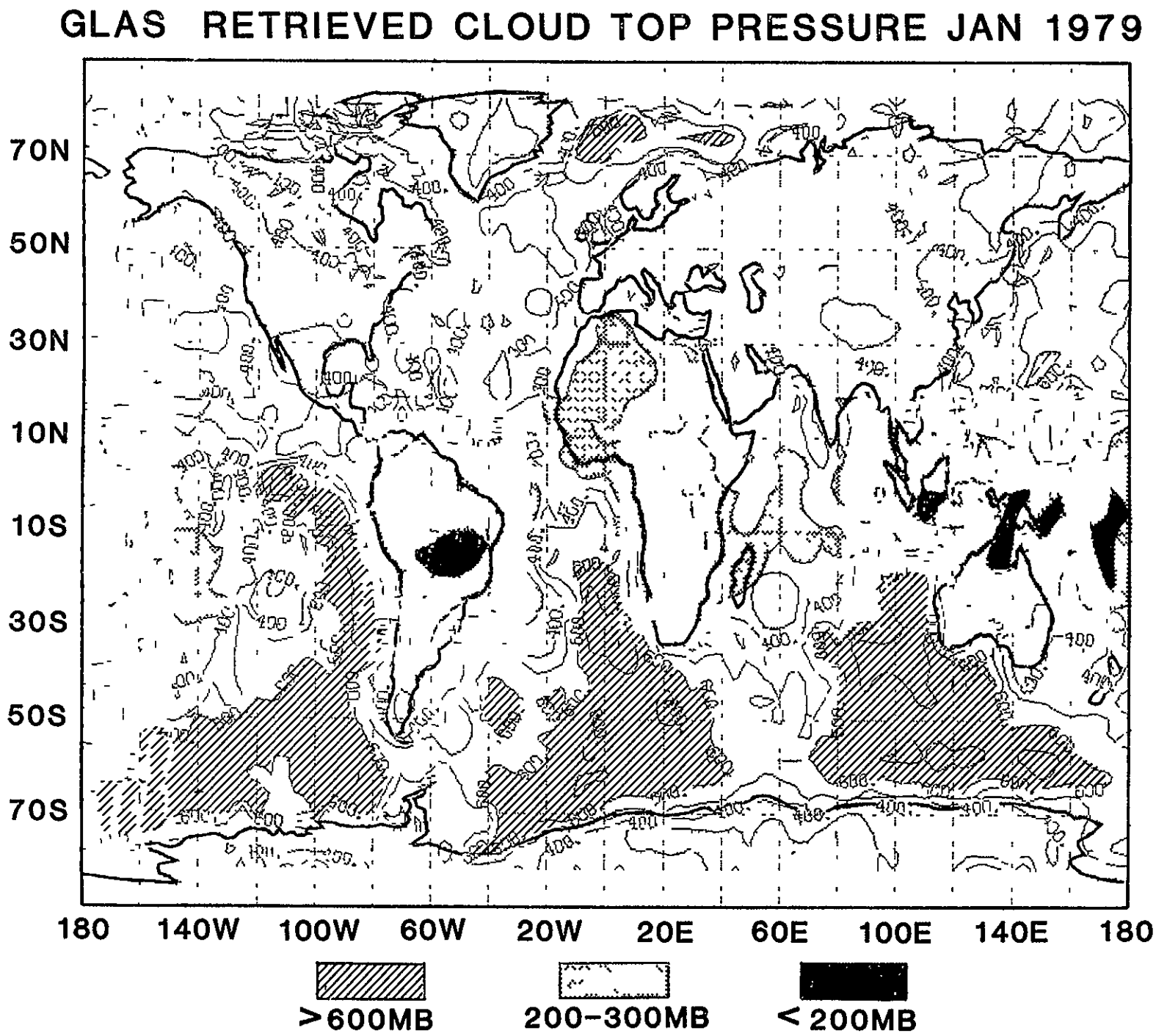

Fig. 9b. Average effective cloud top pressure, weighted by cloud fraction, retrieved by GLAS for January 1979. Only the areas of highest clouds (P_c < 300 mb) and lowest clouds (P_c > 600 mb) are shaded.

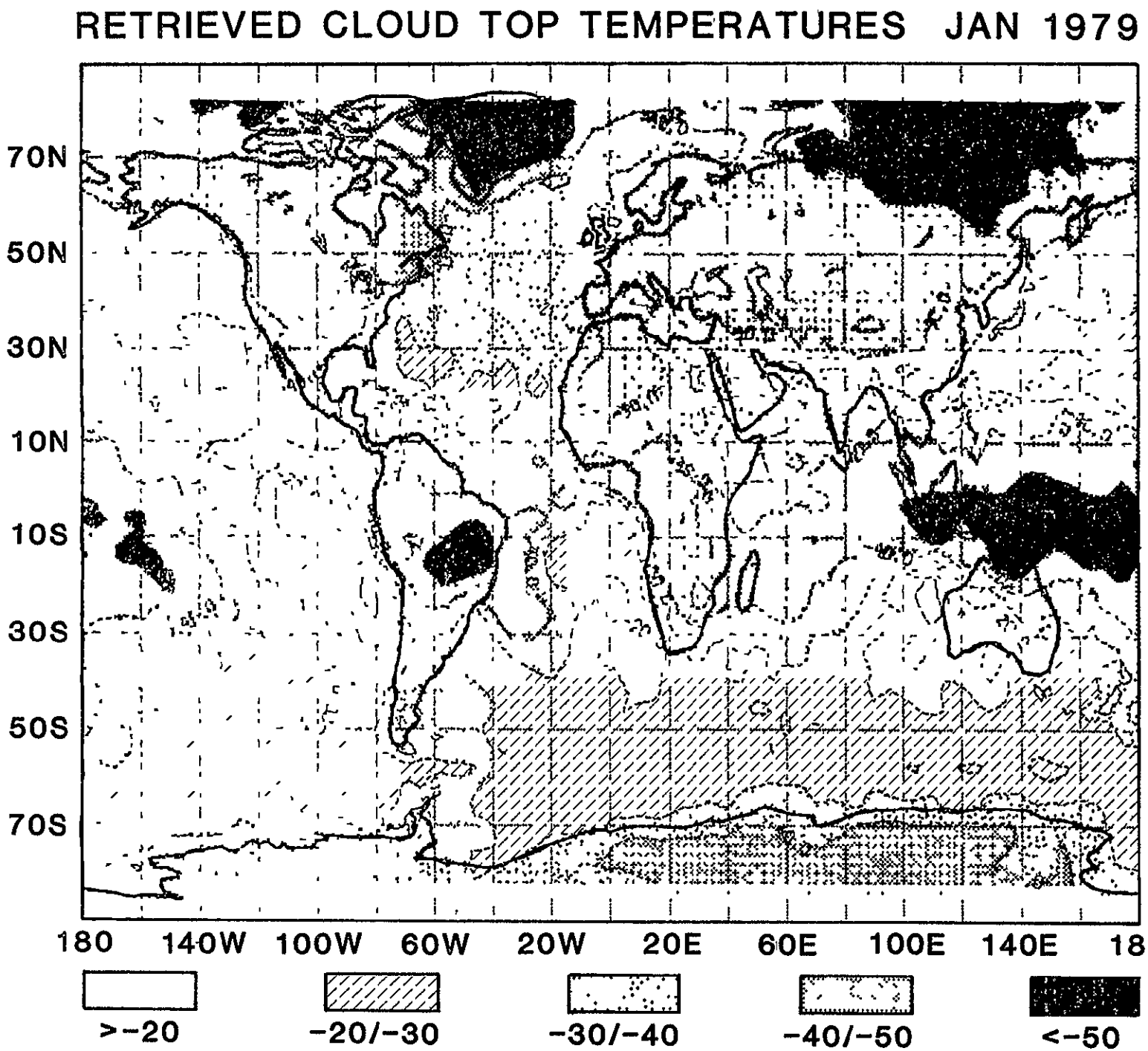

Fig. 9c. Average effective cloud top temperature, weighted by cloud fraction, retrieved by GLAS for January 1979. Temperatures are in °C.

radiation from the warm surface. The major patterns of cloud cover inferred from AVHRR, and determined from the HIRS/MSU system, agree almost perfectly in the tropics. In the extra-tropics, especially in the northern hemisphere winter over land where cold land temperatures exist, and, as shown in Figure (9), cold, though not necessarily extensive, clouds exist, outgoing longwave radiation is not necessarily a measure of cloudiness. Note for example, from Figure (9) that the North Atlantic Ocean is considerably more cloudy than either North America or Eurasia. The outgoing longwave radiation in this area, is higher than that over the continents, however, as shown in Figure (10).

4.5 Microwave Surface Emissivity - Ice and Snow Cover for January 1979

The emissivity of the surface in the microwave region is a strong function of surface conditions. At 50 GHz, open ocean has emissivity values ranging from .45-.65. The emissivity increases with decreasing temperature and also increases with increasing foam cover which is a measure of wind speed [Wilheit, 1979]. Land has emissivities typically greater than .9. Ice over ocean would have an emissivity of the order of .7 for old ice, .9 for new ice, and .7 or more for mixture of new ice and open ocean. Snow over land would have an emissivity of the order of .90 or less [Staelin, 1981]. Thus, the surface emissivity can give a measure of snow cover land, ice cover over ocean, and possibly also boundary layer windspeed over open ocean.

Passive microwave sounders designed to measure surface properties, such as ESMR and SMMR, have used frequencies less than 40 GHz so as to avoid attenuation by atmospheric oxygen, which mixes atmospheric effects into the signal. Use of equation (3.1) accounts for atmospheric effects, and also allows for the incorporation of surface temperatures, obtained from the infra-red 3.7μm channels, into the determination of surface emissivity from the HIRS2/MSU system. The spatial resolution of MSU is considerably lower than that of ESMR or SMMR

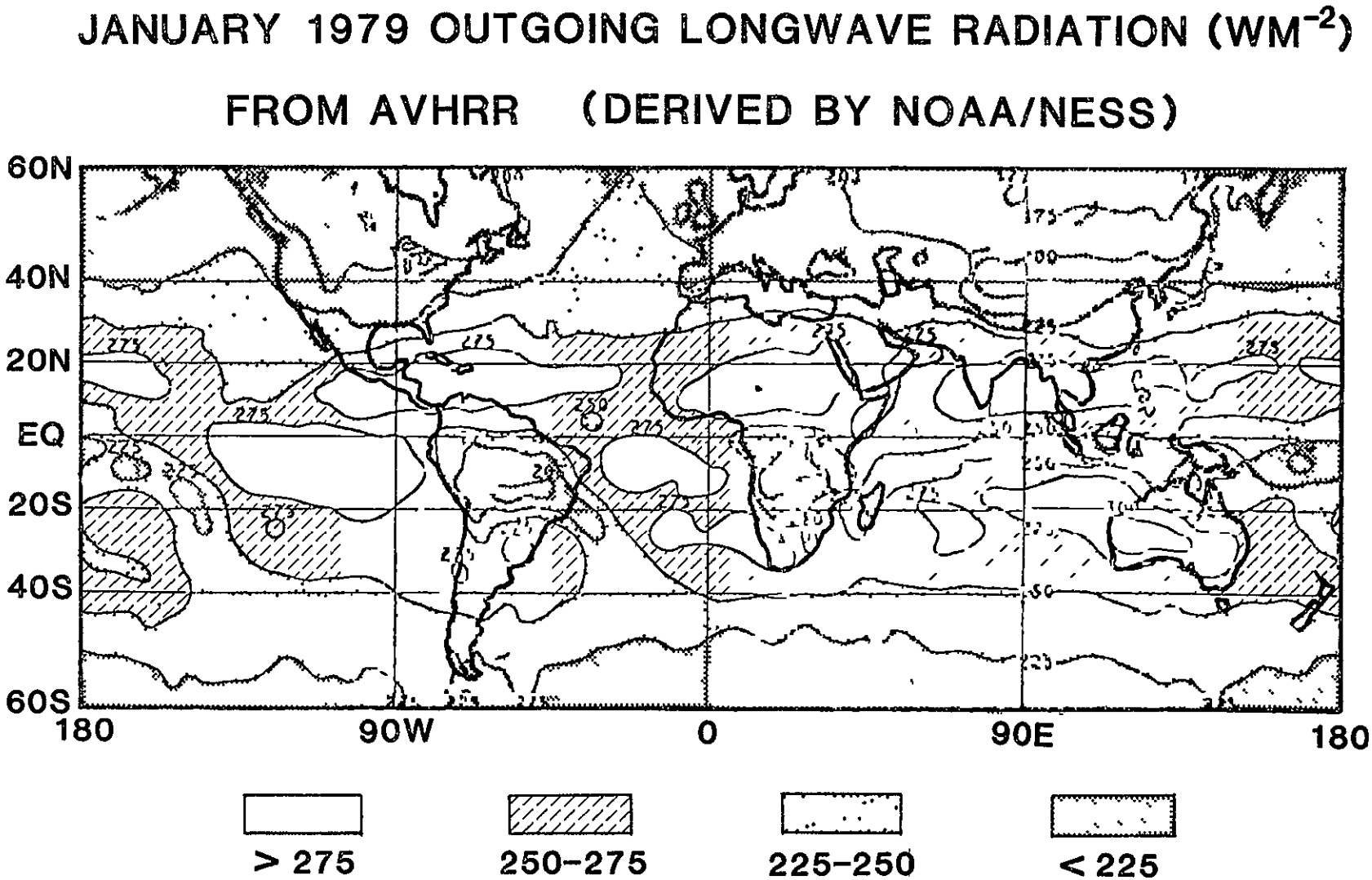

Fig. 10. Outgoing longwave radiation field for January 1979 derived by NOAA/NESS from the 11μm window AVHRR data on 3 A.M. and 3 P.M. observations.

however, and this will degrade high resolution features which could be significant for some applications.

Figure (11) shows the surface emissivity, averaged over the 4° x 5° grid for January 1979. As expected, the most obvious features are the continents, showing rapid gradients from .9 - .6. The intermediate emissivity values are partially due to contouring, and partially due to soundings with mixed fields of view at the coastlines. The emissivity in South America, Africa, and Australia is uniformly greater than .9. North America, Eurasia, and Antarctica show complicated patterns containing lower emissivities, indicative of snow cover.

The oceans show the generally expected features of emissivity between .45 and .65, with emissivity increasing with decreasing sea surface temperature. A distinct .7 contour, indicated by the solid line in the Figure (11), is observed in the Antarctic Ocean and in the Bering, Labrador, Greenland, and Barents Seas. We interpret this contour to be a measure of the sea ice extent in these areas. We have no verification of sea ice in the Antarctic but do have a sea ice field produced from SMMR in the northern hemisphere [Cavalieri, 1981]. Figure (12a) shows the sea ice line as deduced from HIRS2/MSU by the .7 emissivity contour over water. Figure (12b) shows the sea ice line determined from SMMR, with a 25 km resolution. The ice margin from the SMMR data was taken as the contour of sea ice coverage greater than 40%. The agreement is quite good, considering the difference in resolution of the instruments.

The details of the emissivity over land may be indicative of snow cover. Figure (13a) shows the averaged surface emissivity over North America. The .7 emissivity contours, indicative of the onset of significant amounts of sea ice, and the .9 contour, indicative of typical snow free land, are marked. Most of North America has land emissivities less than .9. Figure (13b) shows a map of monthly mean ice and snow cover derived by averaging the weekly observations

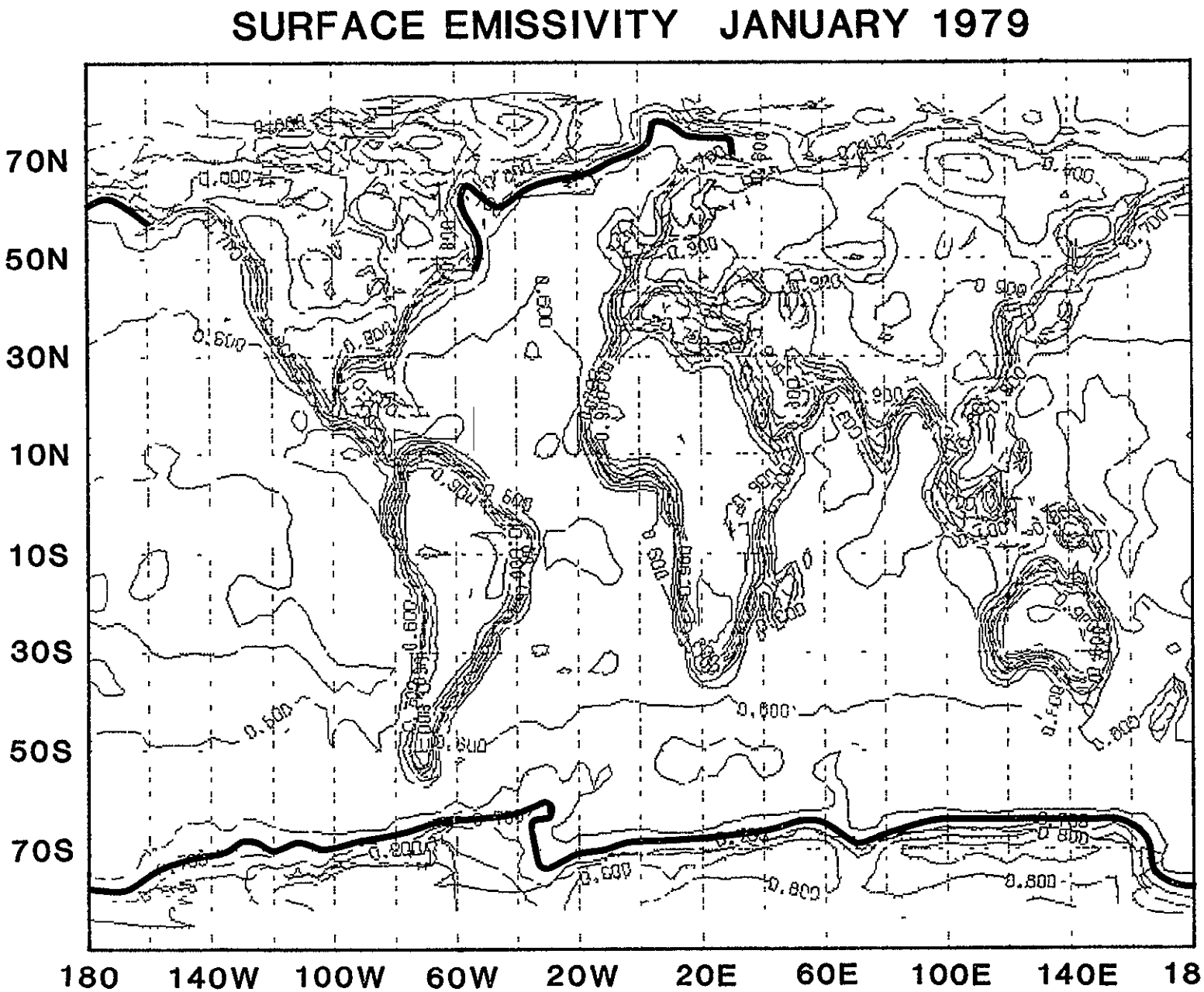

Fig. 11. The average global surface emissivity at 50.3 GHz derived by GLAS for January 1979. Resolution is at the 4° x 5° grid. Emissivities for all the zenith angles of MSU have been averaged together without correction for angle. The .7 emissivity contour over ocean is indicated by the dark line. This contour is taken to be indicative of sea-ice extent.

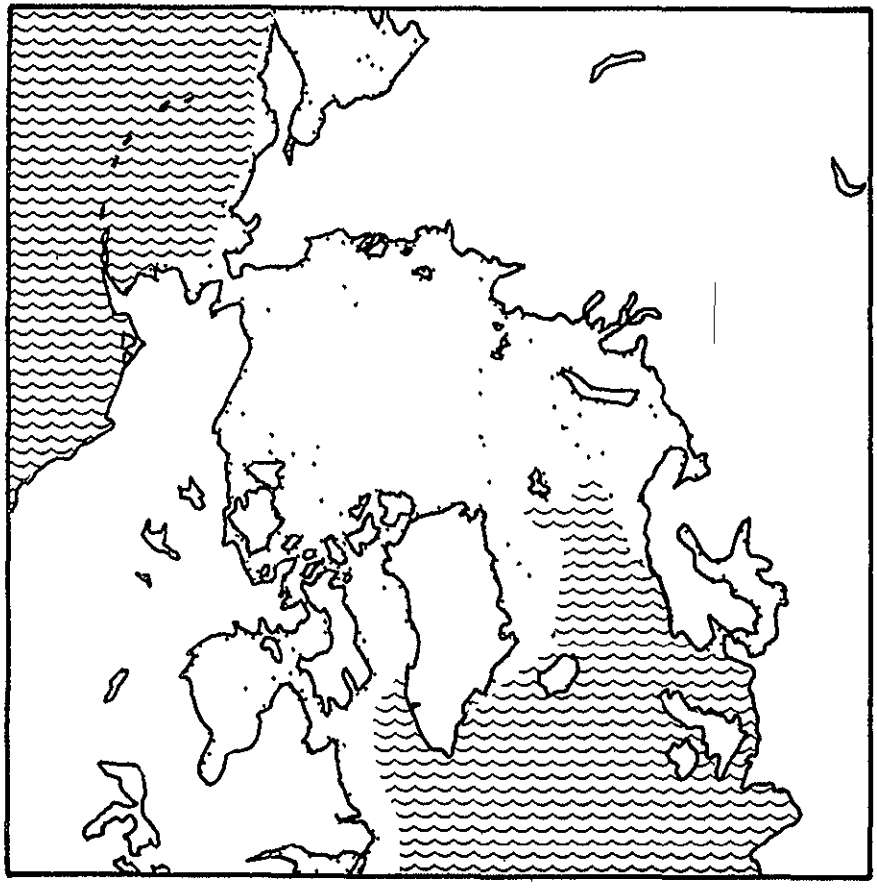

Fig. 12a. North Polar projection showing average sea-ice extent for January inferred from the .7 emissivity contour shown in Fig. 11. Sea ice is indicated by the dots; open ocean by the waves. The MSU spot size is 125 x 125 km at nadir.

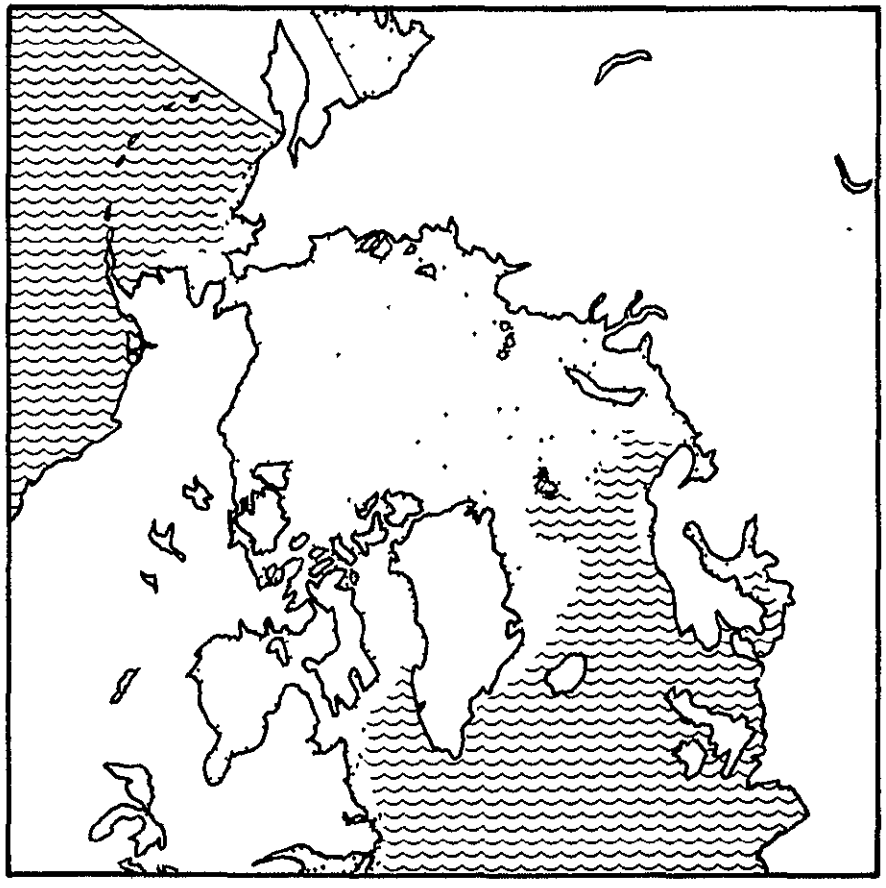

Fig. 12b. Sea ice extent for January 1979 inferred by Cavelieri (1981) from analysis of SMR data, with a 25 x 25 km resolution. The ice/ocean line was taken as the line which represented 40% ice cover for the period

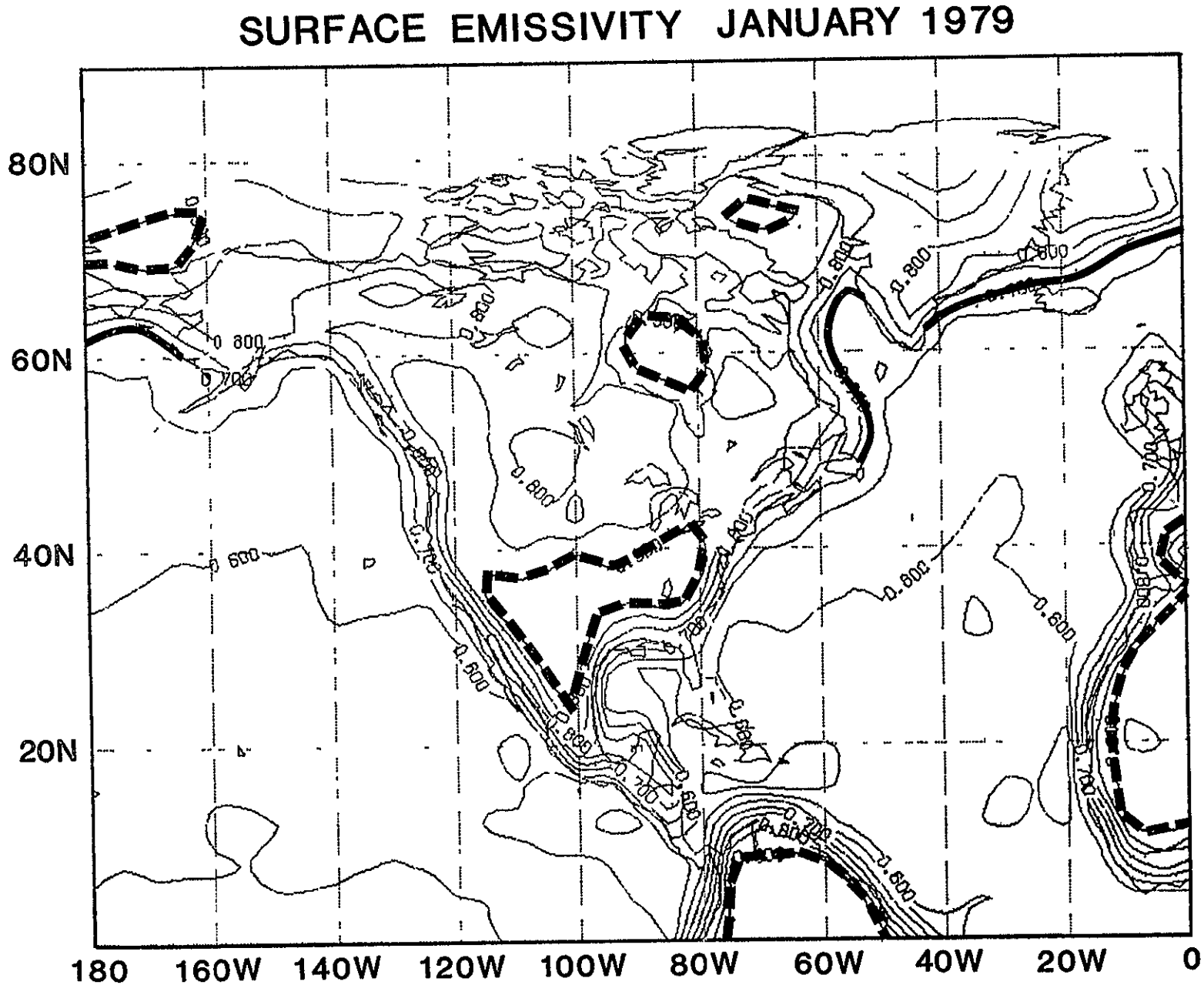

Fig. 13a. Blowup of the northwest quadrant of Fig. 11. The .7 emissivity contour over ocean, indicative of sea ice extent, is shown as the solid line, as in Fig. 11. The .9 contour, indicative of land is shown as the dashed line. Near ocean, it represents the land boundary. Inland, as in North America, it is indicative of the onset of snow-covered land. Further north, it is indicative of solid newly frozen sea ice.

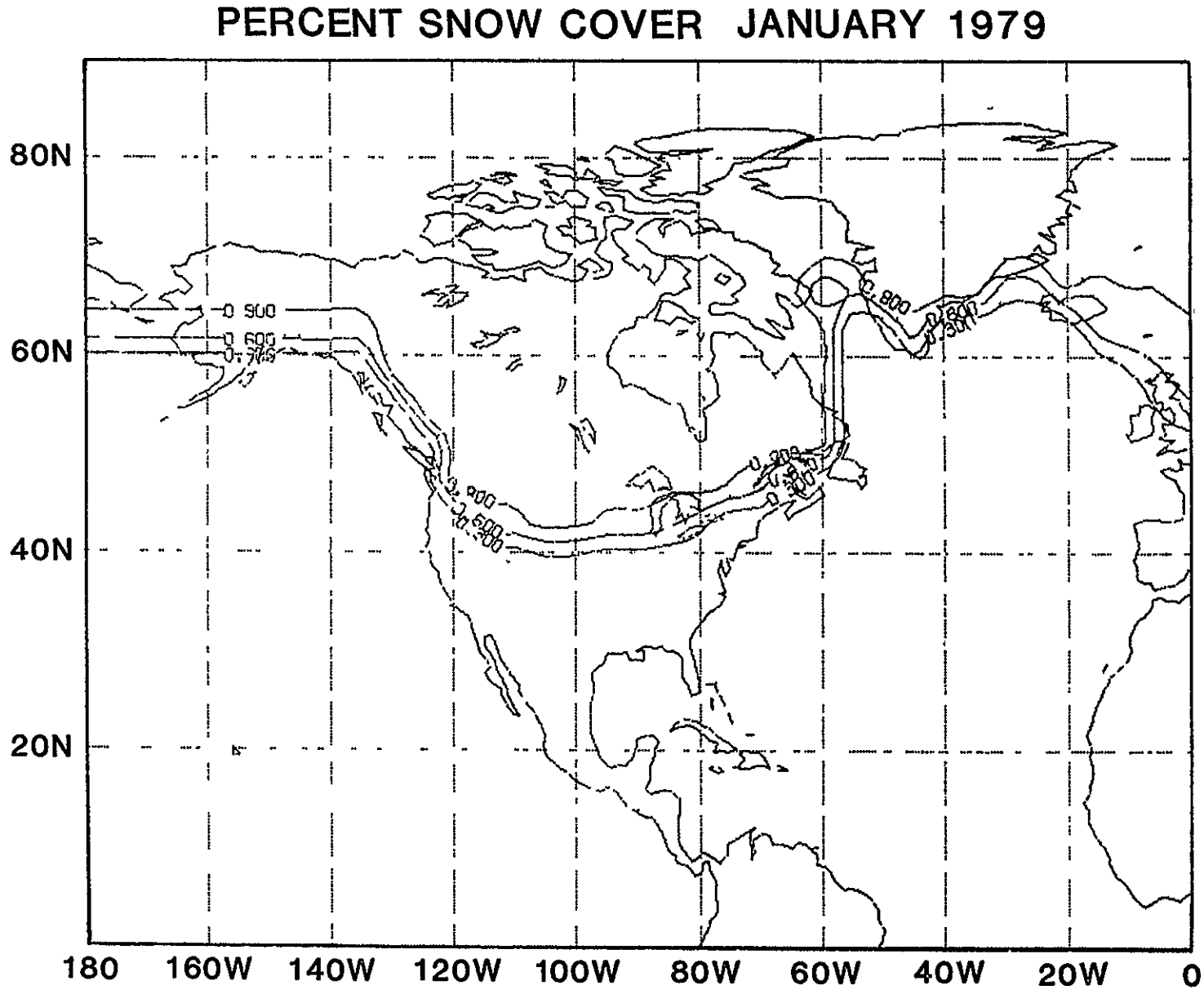

Fig. 13b. Percent snow cover for January 1979 obtained from the NOAA data of Dewey and Heim (1981). The contours indicate the areas of 30%, 60% and 90% snow cover for January 1979.

produced operationally by NOAA/NESS [Dewey and Heim, 1981] into the 4° x 5° grid boxes for the month of January. The .9 emissivity contour lies completely in the snow free area while the .85 contour closely approximates the 60% snow cover contour, indicated in Figure (13b). Detailed studies will be conducted to quantify the relationship between snow cover and ice cover and surface emissivity at 50.3 GHz, including the ability to distinguish between old and new ice and to estimate snow depth. The ability to get qualitative snow and ice snow maps from the operational TIROS-N sounding system is well demonstrated by the current results.

4.6 Summary

The GLAS processing system for analysis of HIRS2/MSU data by finding atmospheric and surface conditions which are solutions to the multispectral radiative transfer equations has been shown to produce not only atmospheric temperature profiles of higher accuracy than those produced operationally during the same period, but also to produce monthly mean fields of surface temperature, cloud properties, and ice and snow cover which show reasonable agreement with ground truth. Simultaneous analysis of infra-red and microwave observations enhances the strength of observations in each spectral region. Infra-red soundings have higher sensitivity to lower tropospheric temperatures and ground temperatures. Microwave observations are better for sounding the stratosphere, are sensitive to snow and ice cover, and greatly aid in correcting the infra-red observations for cloud effects.

The retrieval system has the potential of improving the impact of HIRS2/MSU data on mid-range forecasting (Halem et al., 1982) both because of improved accuracy of the retrievals and also because the retrieval process can be coupled directly into the forecast/assimilation cycle, using the current forecast as a first guess. This provides an analyzed field which is consistent not only

with conventional observations but also with satellite radiance observations as well. The monthly mean fields can form the basis for a long term climatology data base, derived from similar instrumentation, starting from 1979 and continuing through the 80's. Modifications to the processing system are currently being made, based on subsequent research and experience gained from analysis of the products of the current system. The improved system, as well as new results, will be described in a future publication.

References

Barnett, T. P., W. C. Patzert, S. C. Webb, and B. R. Bean, 1979: Climatological usefulness of satellite determined sea-surface temperatures in the tropical Pacific, Bull. Am. Meteorol. Soc., 60, 197-205.

Cavalieri, D., 1981: Unpublished data, private communication.

Chahine, M. T., 1968: Determination of the temperature profile in an atmosphere from its outgoing radiance. J. Opt. Soc. Amer., 58, 1634-1637.

Chahine, M. T., 1970: Inverse problems in radiative transfer: determination of atmospheric parameters. J. Atmos. Sci., 27, 960-967.

Chahine, M. T., 1974: Remote Sounding of Cloudy Atmospheres. I. The single cloud layer. J. Atmos. Sci., 31, 233-243.

Chahine, M. T., 1980: Infra-red Remote Sounding of Sea Surface Temperature Remote Sensing of Atmospheres and Oceans, pp. 411-435. A Deepak, Editor, Academic Press, New York, NY.

Chahine, M. T., 1982: Remote sensing of cloud parameters. J. Atmos. Sci., 39, 159-170.

Chahine, M. T., and J. Susskind, 1982: Determination of the Horizontal and Vertical Distribution of Clouds from Infrared Satellite Sounding Data. Digest Vol. I. IEEE 1982 International Geoscience and Remote Sensing Symposium pp. 3.1-3.5. June 1-4, Munich, Federal Republic of Germany.

Chedin, A., 1982: Private Communication.

Coffey, M. T., and A. Goldman, 1981: Atmospheric Hydrogen Cyanide Absorption Near 14 μm. Appl. Opt., 20, 3480.

Dewey, K. F. and R. Heim Jr., 1981: Satellite observation of variations in Northern Hemispher seasonal snow cover. NOAA Technical Report NESS 87. National Earth Satellite Service, Washington, D. C.

Gruber, A. and M. Varnadore, 1981: Unpublished data, private communication.

Halem, M. and J. Susskind, 1977: The GISS VTPR Processing Manual. NASA Report X-130-77-53. Goddard Space Flight Center, Greenbelt, MD 20771.

Halem, M., M. Ghil, R. Atlas, J. Susskind, and W. Quirk, 1978: The GISS Sounding Temperature Impact Test. NASA Technical Memorandum 78063, pp 2-9 to 2-82. Goddard Space Flight Center, Greenbelt, MD 20771.

Halem, M., E. Kalnay, W. E. Baker, and R. Atlas, 1982: An assessment of the FGGE satellite observing system during SOP-1. Bull. Am. Meteorol. Soc., 63, 407-426.

Horel, J. D. and J. M. Wallace, 1981: Planetary-scale atmospheric phenomena associated with the Southern Oscillation. Mon. Wea. Rev., 109, 813-829.

Jastrow, R. and M. Halem, 1973: Accuracy and coverage of temperature data derived from the IR radiometer on the NOAA 2 satellite. J. Atmos. Sci., 30, 958-964.

Kalnay-Rivas, E., A. Bayliss, and J. Storch, 1977: The 4th order GISS model of the global atmosphere. Beitr. Phys. Atmos., 50, 299-311.

Kalnay-Rivas, E. and D. Hoitsma, 1979: The effect of accuracy, conservation, and filtering on numerical weather forecasting. Preprints, Fourth Conference on Numerical Weather Prediction (Silver Spring) AMS, Boston, pp 302-312.

Kornfield, J. and J. Susskind, 1977: On the effect of surface emissivity on temperature retrievals. Mon. Wea. Rev., 105, 1605-1608.

Lauritson, L., G. Nelson, and F. Porto, 1979: Data extraction and calibration of TIROS-N/NOAA radiometers. NOAA Technical Memorandum NESS 107. National Environmental Satellite Service, Washington, D. C.

McClain, E. P., 1981: Split window and triple-window sea surface temperature determinations from space. Preprint, 1981 ICES Statutory Meeting, Woods Hole, MA., 6-10 October.

McClatchey, R., W. S. Benedict, S. A. Clough, P. E. Burch, R. F. Calfee, K. Fox, L. S. Rothman and J. S. Garing, 1973: AFCRL Atmospheric Absorption Line Parameter Compilation. AFCRL-TR-73-0096. Air Force Cambridge Research Laboratories, Hanscom Field, Bedford, Massachussets 01731.

McClatchey, R. 1976: Satellite Temperature Sounding of the Atmosphere: Ground Truth Analysis. AFGL-TR-76-0279. Air Force Geophysical Laboratory, Hanscom AFB, Bedford, Massachusetts 01731.

McMillin, L. M. and H. E. Fleming, 1976: Atmospheric Transmittance of an Absorbing Gas: A Computationally Fast and Accurate Transmittance Model for Absorbing Gases with Constant Mixing Ratios in Inhomogeneous Atmospheres. Appl. Opt., 15, 358-363.

McMillin, L. M., H. E. Fleming, and M. L. Hill, 1979: Atmospheric Transmittance of an Absorbing Gas 3: A Computationally Rast and Accurate Transmittance Model for Absorbing Gases with Variable Mixing Ratios. Appl. Opt., 18, 1600-1606.

McMillin, L. M. and C. Dean, 1982: Evaluation of a New Operational Technique for producing clear radiances. J. Appl. Meteor., 21, 1005-1014.

Paltridge, G. W. and C. M. R. Platt, 1976: Radiative Processes in Meteorology and Climatology. Elsevier Scientific Publishing Co. Amsterdam-Oxford-New Yor, pp 3, 6, 206.

Phillips, N., L. McMillin, A. Gruber, and D. Wark, 1979: An Evaluation of Early Operational Temperature Soundings from TIROS-N. Bull. Amer. Meteor. Soc., 60, 1188-1197.

Rasmusson, E. M. and T. H. Carpenter, 1982: Variations in tropical sea surface temperature and surface wind fields associated with the Southern Oscillation/ El Nino. Mon. Wea. Rev., 110, 354-384.

Rosenkranz, P. W., 1975: Shape of the 5mm Oxygen band in the atmosphere. IEEE Trans on Antennas and Propa, 23, 498-506.

Rothman, L. S., 1978: Update of the AFGL Atmospheric Absorption Line Parameters Compilation. Appl. Opt., 17, 3517-3518.

Smith, W. L., 1968: An Improved Method for Calculating Tropospheric Temperature and Moisture From Satellite Radiometer Measurements. Mon. Wea. Rev., 96, 387-396.

Smith, W. L., 1970: Iterative solution of the radiative transfer equation for the temperature and absorbing gas profile of an atmosphere. Appl. Opt., 9, 1993-1999.

Staelin, D., 1981: Private communication.

Susskind, J., 1975: Effective H_2O Transmittances in the 15 μm Region. Proceedings of Remote Sensing of the Atmosphere paper WB6. Optical Society of America. March 19-21, Anaheim, California.

Susskind, J. and J. E. Searl, 1978: Synthetic Atmospheric Transmittance Spectra Near 15μm and 4.3μm. J. Quant. Spect. Rad. Trans., 19, 195-215.

Susskind, J. and T. Mo, 1978: Atmospheric Absorption Spectra near 2200 cm^{-1} and 2400 cm^{-1}. AMS Third Conference on Atmospheric Radiation pp. 219-222. Davis, CA., June 28-30, 1978.

Susskind, J. and A. Rosenberg, 1980: Temperature retrievals from TIROS-N Remote Sensing of Atmospheres and Oceans. pp 45-66. Academic Press, New York, N.Y.

Susskind, J. and J. Rosenfield, 1980: The GLAS physical inversion method for analysis of TIROS-N data. VAS Demonstration Sounding Workshop, NASA Conference Publication 2147, pp 41-55. NASA/Goddard Space Flight Center, July 15, 1980.

Valovcin, Francis R., 1981: A Ground Truth Analysis of DMSP Water Vapor Radiances. AFGL-TR-81-0323. Air Force Geophysical Laboratory, Hanscom AFB, Bedford, MA 01731.

Wang, W. C., and G. Domoto, 1974: The Radiative Effect of Aerosols in the Earth's Atmosphere. J.A.M., 13, 521-534.

Wang, W. C., 1975: Private Communication.

Weinreb, M. P. and A. C. Neuendorffer, 1973: Method to Apply Homogeneous Path Transmittance Models to Inhomogeneous Atmospheres. J. Atmos. Sci., 30, 662-666.

Weinreb, M., 1979: Atmospheric Transmission for Remote Temperature Sounding. SPIE, 195, Atmospheric Effects on Radiative Transfer, 22-30.

Wilheit, T. J. Jr., 1979: A model for the microwave emissivity of the ocean's surface as a function of wind speed. IEEE Trans. Geoscience Electronics, 17, 244-249.

Wolfe, W. L., 1965: Handbook of Military Infra-red Technology. U.S. Government Printing Office, Washington, DC.

Wolfe, W. L., and Zissis, G. J., 1978: The infra-red handbook. Office of Naval Research, Dept. of the Navy, Washington, D. C.

BIBLIOGRAPHIC DATA SHEET

1. Report No.	2 Government Accession No	3 Recipient's Catalog No
TM 84936		

4 Title and Subtitle	5 Report Date
THE GLAS PHYSICAL INVERSION METHOD FOR ANALYSIS OF HIRS2/MSU SOUNDING DATA	November 1982
	6. Performing Organization Code
7 Author(s) J. Susskind, J. Rosenfield, D. Reuter, M. T. Chahine	8. Performing Organization Report No
9 Performing Organization Name and Address	10 Work Unit No
NASA Goddard Space Flight Center Greenbelt, Maryland 20771	11. Contract or Grant No
	13. Type of Report and Period Covered
12 Sponsoring Agency Name and Address	
	14 Sponsoring Agency Code

15 Supplementary Notes

16. Abstract

GLAS has developed a method to derive atmospheric temperature profiles, sea or land surface temperatures, sea ice extent and snow cover, and cloud heights and fractional cloud, from HIRS2/MSU radiance data. Chapter 1 describes the physics used in the radiative transfer calculations and demonstrates the accuracy of the calculations. Chapter 2 describes the rapid transmittance algorithm used and demonstrates its accuracy. Chapter 3 describes the theory and application of the techniques used to analyze the satellite data. Chapter 4 shows results obtained for January 1979.

17 Key Words (Selected by Author(s))	18 Distribution Statement
Remote Sensing, Radiative Transfer, Temperature Sounding, Climate Data Sets	

19 Security Classif. (of this report)	20 Security Classif (of this page)	21 No of Pages	22 Price*
u	u		

*For sale by the National Technical Information Service, Springfield, Virginia 22151

GSFC 25-44 (10/77)